Bud13 Promotes a Type I Interferon Response by Countering Intron Retention in Irf7

Luke S. Frankiw[1,2], Devdoot Majumdar[1,2], Christian Burns[1], Logan Vlach[1], Annie Moradian[1], Michael J. Sweredoski[1], David Baltimore[1,3*]

[1]*Division of Biology and Biological Engineering, California Institute of Technology, Pasadena, CA 91125, USA*
[2]*These authors contributed equally*
[3]*Lead Contact*
**Correspondence: baltimo@caltech.edu*

SUMMARY

Intron retention (IR) has emerged as an important mechanism of gene expression control. Despite this, the factors that control IR events remain poorly understood. We observed consistent IR in one intron of the Irf7 gene and identified Bud13 as an RNA-binding protein that acts at this intron to increase the amount of successful splicing. Deficiency in Bud13 led to increased IR, decreased mature Irf7 transcript and protein levels, and consequently to a dampened type I interferon response. This impairment of Irf7 production in Bud13-deficient cells compromised their ability to withstand VSV infection. Global analysis of Bud13 knockdown and BUD13 cross-linking to RNA revealed a subset of introns that share many characteristics with the one found in Irf7 and are spliced in a Bud13-dependent manner. Deficiency of Bud13 led to decreased mature transcript from genes containing such introns. Thus, by acting as an antagonist to IR, Bud13 facilitates the expression of genes at which IR occurs.

INTRODUCTION

Three forms of alternative processing of a pre-mRNA have been described: differential inclusion of an exon, alternative splice site selection, and intron retention (IR). The latter, IR, has emerged as a previously underappreciated mechanism of post-transcriptional gene regulation. Unlike the two alternative splicing events, IR rarely contributes to proteomic diversity.[1] However, IR events have the ability to act as negative regulators of gene expression by: (1) delaying onset of gene expression by slowing down splicing kinetics, (2) increasing potential nuclear degradation by nuclear exosomes, (3) increasing potential cytoplasmic degradation by nonsense mediated decay.[2]

Recent genomic studies suggest IR plays an important role in the regulation of gene expression in a wide range of processes including cellular differentiation[3,4] and tumorigenesis.[5] Further, widespread IR throughout mouse and human cell and tissue types has led to the idea that IR events act to functionally "tune" the transcriptome of a cell.[6] However, with few exceptions, the factors that control IR events and thus potentially shape gene expression programs of cells, remain poorly understood.

Irf7 is an interferon-inducible master regulator of the type-I interferon-dependent immune response and is crucial to the production of interferon-α and β.[7] Aberrant Irf7 production is linked to a wide range of pathologies, from life-threatening influenza[8] to autoimmunity[9], because precise regulation of Irf7 ensures a proper immune response. Notably, intron 4 of Irf7 is short, GC-rich, and has a poor splice donor sequence, characteristics shared by many poorly spliced introns. We and others have previously shown that intron 4 of Irf7 splices inefficiently[10], affecting gene expression and opening a new line of inquiry as to the mechanism of IR regulation in *Irf7*.

Using RNA antisense purification-mass spectrometry (RAP-MS)[11], we identified the protein Bud13 as one that regulates IR in Irf7. Bud13 was found to aid splicing efficiency and expression of the Irf7 mature transcript and protein, thus promoting the downstream type-I interferon-dependent immune response. We show that Irf7 is able to trigger a robust interferon response in the presence but not in the absence of Bud13. Further, Bud13 was found to increase the splicing efficiency of a multitude of other junctions with similar characteristics to the one found in Irf7. By aiding in splicing

efficiency, Bud13 limits intron retention and increases gene expression levels of transcripts containing Bud13 dependent junctions.

RESULTS

Irf7 contains an intron that splices poorly following stimulation.

To study the role of mRNA splicing during an innate immune response, we sequenced the RNA from mouse bone marrow-derived macrophages (BMDMs) stimulated with either TNFα, IFNα, or Poly(I:C). From this sequencing, we identified an increased number of intronic reads in the fourth intron of the most abundant transcript of Irf7 (Fig. 1A). A variety of features of this intron make it a likely candidate for retention.[6] It is extremely small at 69 nucleotides and has a high G/C content in both the flanking exons and within the intron itself (Fig. 1B-E). Furthermore, the intron contains a 'weak' 5' splice site, one that deviates significantly from a consensus splice site sequence. This is quantified using a maximum entropy model to calculate the splice site quality score (Fig. 1F).[12] This retention is independent of time or stimulant (Fig. 1G, H).

To quantify the extent of retention across RNA-seq data-sets, we use a metric we designate the "splicing ratio" (SR) (Fig. 1I; see methods), which is a length normalized ratio of intronic reads to total reads at each junction. Low SR values indicate a junction is primarily spliced whereas high SR values indicate a junction is primarily unspliced. Using this metric, we quantified the extent of retention for all junctions in the most abundant Irf7 transcript. We observed that for all types of stimulation, the retention of the fourth intron of the transcript is much greater than that seen for any of the other introns (Fig. 1J and S1A, B). This intron remains poorly spliced despite the fact that there is clear excision of neighboring introns. It is worth noting that quantitation of the IFNα stimulation shows increased intronic signal throughout the Irf7 transcript. This increased intronic signal is due to faster and stronger induction of Irf7 via stimulation with IFNα and as such, an increase in the amount of pre-mRNA at a given stimulation time-point. Despite this increase in intronic signal throughout the transcript, we observed a corresponding increase in the level of

retention for the poorly spliced fourth intron (Fig. 1J, S1B). Thus, we conclude this intron of Irf7 splices poorly following many forms of stimulation.

RAP-MS identifies Bud13 as an RNA binding protein that interacts with IRF7 mRNA.

To understand how cells handle a retained intron, we sought to identify trans-acting proteins that might affect the process using RNA Antisense Purification followed by Mass Spectrometry (RAP-MS) (Fig. 2A)[11]. RAP-MS employs antisense biotin-containing ssDNAs complementary to *Irf7* exons to purify the proteins associated with the total pool of *Irf7* transcripts, containing both nascent pre-mRNAs and mature mRNA. Using this proteomic approach, we identified the RNA-binding protein Bud13 to be highly enriched (~6-fold) on Irf7 transcripts as compared to β-*actin* transcripts, which were used as a control (Fig. 2B). Bud13 has been characterized in yeast as a member of the Retention and Splicing complex (RES),[13] forming a trimeric complex with Pml1p and Snu17p, and aids in the splicing and nuclear retention of a subset of transcripts. It is not well characterized in mammalian systems. We captured a variety of other known RNA-binding proteins (Pum2, Prpf40a, Son); however, no other protein was enriched greater than two fold on Irf7 transcripts. We observed specificity in the RNA antisense purification for the intended transcripts (Fig. 2C).

Following RAP-MS, we confirmed Bud13 enrichment on Irf7 transcripts by performing RNA Immunoprecipitation (RIP) followed by qPCR. Using formaldehyde cross-linked, BMDMs stimulated with TNFα for 30 minutes or Poly(I:C) for 12 hours, we observed >7-fold enrichment of *Irf7* transcripts associated with Bud13 immunoprecipitates as compared to Rabbit IgG control immunoprecipitates (Fig. 2D, E). Of note, despite using two different stimuli, we find similar levels of enrichment. In contrast, no differential enrichment of Rpl32 was observed. Thus, isolating the proteins associated with Irf7 mRNA transcripts led to the identification of Bud13, and immunoprecipitation of Bud13 protein confirmed enrichment of Irf7 mRNA.

Bud13 knockdown leads to increased retention in the weak Irf7 intron.

To determine whether the enrichment of Bud13 had an effect on Irf7 mRNA processing, we used an shRNA approach to knockdown Bud13 protein levels in BMDMs (Fig. S2A, B). To quantify differences in splicing between the shBud13 sample and the scrambled control sample, we calculated the difference in the previously mentioned splicing ratio (SR) metric between shBud13 and control for each junction at each time point. This resulting value was designated the ΔSR. A positive ΔSR indicates a junction is more unspliced in the shBud13 sample while a negative ΔSR indicates a junction is more unspliced in the control sample.

RNA-seq was performed on RNA from unstimulated BMDMs, as well as macrophages stimulated with TNFα for 0, 30, 60, and 120 minutes. Bud13 knockdown led to a further increased retention of the fourth intron in *Irf7* (Fig. 3A – highlighted intron, S2C). Further, the sequencing coverage plots showed little variation in splicing for the other seven introns in the transcript. This was confirmed when splicing was quantified using the ΔSR metric (Fig. 3B). This splicing difference was confirmed via RT-PCR (Fig. 3C). At all stimulation time-points, the ΔSR value for the fourth intron was significantly greater than 0, indicating an increase in retention when Bud13 levels were reduced. There is a significant difference in the ΔSR of intron 4 as compared to every other junction in the Irf7 transcript ($p<0.001$, Student's t-test). All other pairwise comparisons are insignificant. It appears that Bud13 plays a specific role of aiding in the excision of the poorly spliced junction but is not required for total splicing of other introns in the transcript, at least as indicated by the partial knockdown with an shRNA. We next looked at how this retention affected the induction kinetics of Irf7. We observed decreased induction of Irf7 mRNA in response to TNFα stimulation in shBud13 BMDMs as compared to control BMDMs (Fig. 3D), consistent with the idea that intron retention leads to transcript degradation.[14] Other TNFα induced transcripts that lacked a Bud13 dependent splicing defect showed similar induction between the time-courses (Fig. S2 D-F).

Bud13 knockdown alters the type I interferon response.

Because Irf7 is known as a 'master regulator' for robust type I interferon production[7], we next investigated the effect of Bud13 knockdown on a type I interferon response. To do so, we stimulated BMDMs with the TLR3 agonist Poly(I:C) for up to 24 hours. Activation of TLR3 leads to the production of type I interferons followed by the downstream induction and activation of Irf7, which serves to amplify the type I interferon response via positive feedback[8]. We again observed differential splicing between the shBud13 samples and the control samples in intron 4 of Irf7 (Fig. 4A, S3A). As before, there is a significant difference in the ΔSR of intron 4 as compared to every other junction in the Irf7 transcript (Fig. 4B. $p<0.001$, Student's t-test), whereas all other pairwise comparisons are insignificant. As is the case with TNFα, knocking down Bud13 altered Irf7 induction kinetics. Less Irf7 mRNA is induced at 240, 720, and 1440mins of poly(I:C) stimulation (Fig. 4C). This reduction in Irf7 mRNA leads to a decrease in the amount of Irf7 protein produced (Fig. 4D).

Next we looked at how this reduction in Irf7 would alter the production of RNA from interferon signature genes (ISGs). Expression of 119 ISGs (selected based on upregulation in response to IFNα [15]; see methods) was examined. In unstimulated BMDMs, used as a baseline, the median $\log_2$ expression fold change (FPKM shBud13/ FPKM control) is 0.1655 (Fig. 4D). In contrast, at 720 mins of stimulation, the median $\log_2$ expression fold change shifts to -0.1007 (Fig. 4E), indicating a significant decrease in ISG expression in the shBud13 sample compared to the control sample at this time-point compared to the baseline (Wilcoxon rank-sum, $P< .001$). This significant decrease in ISG expression remained true when comparing any of the 'early' time points (0, 15, 60 mins) to any of the 'late' timepoints (240, 720, 1440 mins) (Fig. 4G, Wilcoxon rank-sum, $P<0.001$). qPCR was used to monitor expression of both IFNα and IFNβ following 720 and 1440 mins of Poly(I:C) stimulation. We observed significant reduction in both when comparing the shBud13 samples as to the control samples (Fig. 4H, I). To ensure differential expression of ISGs was not due to splicing defects from Bud13 knockdown, we quantified the ΔSR for every ISG junction at 720 mins. The fourth intron of Irf7 has the greatest ΔSR at 0.227. Only four other junctions of the 375 that were examined have ΔSRs greater

than 0.1, and the majority of junctions have ΔSRs close to 0 (Fig. S3C; mean = 0.002, median = 0). Similar results were obtained when BMDMs were stimulated with the TLR9 agonist CpG (Figure S4). Taken together, we conclude that Bud13 deficiency results in a highly compromised type I interferon response.

We next examined whether Irf7 pre-mRNA with a retained fourth intron was able to exit the nucleus and enter the cytoplasm. BMDMs were stimulated with poly(I:C) and fractionated into a nuclear fraction (containing the nucleoplasm and chromatin) and a cytoplasmic fraction. RNA-seq was performed on both fractions. In the cytoplasm, we found Irf7 mRNA to be completely spliced (Fig. 4J, K). Thus, unspliced Irf7 is either being degraded in the nucleus, or it makes it to the cytoplasm and is degraded extremely quickly, such that virtually no signal can be detected via RNA-seq. Furthermore, in support of our whole cell sequencing data and Irf7 immunoblots, we observed less Irf7 mRNA in the cytoplasm in shBud13 samples as compared to control samples (Fig. 4L). In the nucleus, although we notice a large number of unspliced reads at all junctions in both samples, the fourth intron of Irf7 again showed a specific dependency on Bud13 (Fig. 4K, S5B). Finally, the fourth intron had a greater RPKM in the nucleus in shBud13 compared to control BMDMs across the stimulation time-course (Fig. 4K) and had a significantly greater nuclear ΔSR than any other junctions in the transcript (Fig S5B).

Global analysis of the role of Bud13 in BMDMs.

We next investigated global splicing differences caused by Bud13 knockdown. Using the TNFα stimulated data-set, ΔSR was calculated for every junction in every expressed gene. We found that a number of other transcripts had a Bud13 dependent junction (Fig. 5A). Of note, the fourth intron of Irf7 is among the most Bud13 dependent junctions in both the TNFα and Poly(I:C) data-sets (Fig. 5A., Fig. S6H, see methods for analysis details). Similar to the case with Irf7, almost all transcripts contain only a single Bud13 dependent junction, even when low thresholds are used to quantify dependency (Fig. 5B). To determine whether splicing differences caused by Bud13 knockdown led to altered gene expression, we compared the effect of the Bud13 knockdown on

genes that contained a Bud13 dependent junction to those that did not. (see methods). The median $\log_2$ expression fold change (FPKM shBud13/ FPKM control) for genes containing a Bud13 dependent junction was -0.5084. In contrast, the median $\log_2$ expression fold change (FPKM shBud13/ FPKM control) for genes without any junctions affected by Bud13 knockdown was -0.2170. Thus, we conclude there is an inverse relationship between IR due to Bud13 knockdown and gene expression (Wilcoxon rank-sum, $P < .01$) (Fig. 5C).

Next, it was of interest to us to identify sequence elements that led Bud13 to have its specific splicing effect. The most evident element to explore was the effect of splice site strength on Bud13-dependent splicing. Previous work has shown that the yeast orthologue of Bud13 plays a role in efficient splicing for a junction with a weak 5' splice site[13]. Further, the junction affected in Irf7 has a non-consensus 5' splice site. To investigate this issue, we first quantified every 5' and 3' splice site using a maximum entropy model.[12] Then, we took progressively weaker splice site thresholds, and compared the mean ΔSR for every junction below that threshold to the mean ΔSR of every junction in the data-set (Fig. 5D). We saw that as the splice site threshold for the 5' splice site became progressively weaker, the mean ΔSR for junctions weaker than that threshold increased and thus there was a greater Bud13 splicing effect. This result was not seen when the same analysis was applied to the 3' splice site. In support of a 5' splice site dependency for a Bud13 effect, we noticed differences in the 5' splice site motif of Bud13 dependent junctions as compared to to all expressed junctions (Fig. 5E).

We then analyzed the Bud13 splicing effect with respect to other features known to correlate with IR.[6] Across all time-points for both TNFα (Fig. 5F-H) and Poly(I:C) (Fig. S7 A-C), Bud13 dependent introns were dramatically smaller and had increased G/C content in both the intron and in the flanking exons. We also noticed that the distance from the branch point to the 3' splice site was smaller in the Bud13 dependent introns than in the total data-set (Fig. 5I, Fig. S7D). This could be a byproduct of the smaller intron length; however, it is of interest because Bud13 has been shown in yeast to bind just downstream of the branch point.[16] A significant difference was not seen in branch point strength and Bud13 splicing effect (Fig. S7 E, F). As IR is only one form of alternative splicing,

we also looked at whether other forms of alternative splicing were affected by Bud13 knockdown. We found that the most statistically significant number of alternative splicing events were IR events (Fig. S7G, see methods). There were three-times as many IR events as the next most alternative splicing event. IR at intron 4 in Irf7 was the only alternative splicing event that occurred in transcripts related to the type I interferon response.

eCLIP shows enrichment on Bud13 dependent junctions near the 3' splice site.

Next we used enhanced crosslinking and immunopreciptation (eCLIP)-seq data from the ENCODE Project Consortium[17] to investigate Bud13 binding specificity across the genome. We found that in K562 and Hep G2 cells, the majority of Bud13 eCLIP-sequencing reads were located downstream of the branchpoint near the 3' splice site (Fig. 6A, B), consistent with what is seen in yeast.[16] Plots are shown as a measure of binding over input. There is some read density near the 5' splice site, which we hypothesize is due to Bud13's association with the spliceosome. Although it may not bind near the 5' splice site, factors in the spliceosome that interact with Bud13 may immunoprecipitate with Bud13, leading to 5' signal. Data for Sf3b4 and Prpf8, known RBPs that interact with the 3' and 5' splice site respectively, is also shown for comparison (Fig. 6A, B). We hypothesized that Bud13 binding would correlate with Bud13 activity. To test this hypothesis, we used knockdown data from the ENCODE Project Consortium to determine Bud13 dependent junctions in K562 and Hep G2 cells. In K562 cells, we noticed that there was a significant increase in Bud13 binding over input at Bud13 dependent junctions (Fig. 6A). In Hep G2 cells, this increase was less pronounced (Fig. 6B), however, we note that we found Bud13 knockdown had a much greater impact in K562 cells as compared to Hep G2 cells (Fig. S8A). In order to survey a large enough selection of junctions in Hep G2's, we had to significantly lower our threshold for what was deemed a Bud13 dependent junction (see methods), which in turn might explain the dampened Bud13 binding/activity relationship in Hep G2. We conclude that Bud13 either preferentially associates with these Bud13 dependent junctions or associates with them for a longer period of time,.

We next performed peak calling to determine the location of significant peaks. We find the majority of peaks are in intronic regions or intron-exon junctions and that most of the peaks that lie in intron-exon junction are located at the 3' junction (Fig. 6C, D). As might be expected from knockdown data, when comparing introns that have an overlapping eCLIP peak to all introns from expressed transcripts, we see both a length and G/C% bias (Fig. 6E, F). Bud13 peaks tend to fall in smaller introns that are GC rich, a finding consistent with the ΔSR data. Lastly, a list of the GO biological processes most enriched from the list of peaks in K562 and Hep G2 cells is shown (Fig. 6G).

Bud13 knockdown alters the BMDM response to VSV.

Vesicular stomatitis virus (VSV) is a (-)ssRNA virus known to induce type I IFN through TLR7[18]. To test whether impairment of Irf7 due to Bud13 knockdown was present in VSV stimulated BMDMs, we infected both shBud13 and control BMDMs at an MOI of 5 and 10. At all time-points throughout infection in both MOIs, there was dampened Irf7 induction (Fig. 7A, B) as quantified by Taqman qPCR. Next, in order to determine the consequences of impaired Irf7 induction, we determined the yield of virus from BMDMs following a period of infection with a given input MOI. shBud13 BMDMs produce significantly more VSV as compared to control BMDMs (Fig. 7C). This difference in viral production is presumably due to decreased production of Irf7 and the corresponding dampened type I interferon response. To test if a mechanism other than Irf7 intron retention may contribute to the impaired response to viral infection, we rescued Irf7 levels by expressing Irf7 cDNA either in the context of the Bud13 knockdown or the control. We found overexpression of Irf7 cDNA effectively rescues the ability for a cell to clear virus (Fig. 7C). As such, we conclude that the viral susceptibility associated with Bud13 knockdown is due to the increased intron retention in the fourth intron of Irf7 and the corresponding dampened type I interferon response.

DISCUSSION

In this study, we sought proteins that might relate to the poor splicing of an intron in Irf7 transcripts. Using RAP-MS, we identified Bud13 as a protein that has the ability to increase splicing of the Irf7 intron. In the absence of *Bud13*, in response to inflammatory stimulus, macrophages produced Irf7 with increased intron retention (IR) and notably less mature Irf7 transcript and protein (Fig. 3C, 4C, 4D, S4C). Irf7 is the interferon-inducible master regulator of the type-I interferon-dependent immune response.[7] Correspondingly, depletion of Bud13 led to a general reduction in ISG and cytokine production, implying a compromised type I interferon response (Fig. 4E-J, S4D-G). This splicing and corresponding expression defect upon Bud13 depletion was observed under various stimulation regimens and times. We found that macrophages deficient for Bud13 were strikingly more susceptible to infection by VSV, presumably owing to the reduction in Irf7 transcript levels (Fig. 7).

We observed the Bud13 splicing dependence in other introns of other genes. A number of short, GC-rich introns with non-consensus splice donor sites were excised inefficiently when Bud13 levels were depleted (Fig. 5). As was the case with Irf7, this increased IR reduced mature transcript levels (Fig. 5A). Transcripts containing retained introns have been shown in the literature to be degraded by two mechanisms: (1) nuclear degradation via the RNA exosome, (2) cytoplasmic degradation upon detection of a pre-termination codon (PTC) via the NMD decay machinery. Although the majority of these introns contain a PTC, it remains to be determined whether degradation is occurring in the nucleus or cytoplasm.[14,19]

Bud13 was originally identified as a part of a “Retention and Splicing” (RES) complex[13] in yeast. However, yeast Bud13 (ScBud13) and mammalian Bud13 are significantly different lengths (266 vs. 637 amino acids) [20], with only the mammalian protein containing a large, disordered arginine-rich N-terminal domain. ScBud13 counteracts IR in introns within the mediator complex, mating genes, and tRNA modifying genes[21–23], which in turn impair yeast budding. In connection with the RES complex, ScBud13 is thought to safeguard formation of the ‘B^{act} complex’ of the spliceosome.[24] In the B^{act} stage, the 5’ splice donor and branch point are recognized by the

spliceosome. However, progression to catalysis of the first step of the splicing reaction requires remodeling of several spliceosome components.[25] Lack of the RES complex has been shown to lead to premature binding of Prp2, a quality control factor that is responsible for spliceosome remodeling as well as the disassembly of suboptimal substrates. It has been hypothesized that ScBud13 and the RES complex temporally regulate Prp2 binding.[24] In the mammalian context, short, GC-rich introns with weak donor sites may be particularly susceptible to Prp2-mediated disassembly, which may explain the specificity of IR events upon Bud13 depletion.

In yeast, differential studies using mass spectrometry[26] and cross-linking have established that some ScBud13 is detectable in preparations of stalled B, B^{act}, and B* complexes. One cryo-EM structure of the yeast spliceosome found density corresponding to ScBud13 in a stalled B^{act} pre-catalytic complex, although a structure of the stalled B complex found only weak density for ScBud13.[21,27] In mammals, structural evidence of Bud13 is limited. Given the partial sequence homology between all members of the yeast RES complex and their mammalian counterparts, it is not surprising that Bud13 (and other RES complex members) are often undetectable in preparations of stalled spliceosomes using cross-linking and mass-spectrometry. Furthermore, Bud13 was not detected in a recent human cryo-EM structure of a stalled B complex.[28] Taken together, it is not yet possible to determine if the sub-stoichiometric nature of Bud13 in mammalian spliceosome complexes is because it is constitutively associated but highly transient or because it serves as a non-essential accessory to spliceosome function. Cryo-EM studies, as well as single molecule studies, would seem to suggest compositional heterogeneity of the spliceosome, and that the Bud13-endowed spliceosome may catalyze the splicing reaction in a fundamentally different way than is used in its absence.[24,29,30]

Recently, the RES complex in zebrafish was shown to regulate levels of IR in short, GC-rich introns in knockout studies.[31] Indeed, both in Zebrafish[31] and C. Elegans,[32] deficiency of RES components has been reported to lead to embryonic lethality. Our results show that mammalian Bud13 shares this splicing fidelity function, and deficiency may prevent proper development. Despite this, knockdown and knock-out cell lines have displayed no overt growth defects, suggesting a

developmental but not immune-cell intrinsic dependence on Bud13 for survival. Of note, we did sequence knockdowns of the other RES components, Rbmx2 and Snip1 (Fig. S11). We see a very mild effect on the fourth intron of Irf7, and although the fourth intron is the most affected in both cases as measured by ΔSR, it lacks statistical significance when compared to other introns in the transcript. Further, we find very mild global IR when compared to the IR induced by Bud13 knockdown. We do not believe our data disputes what is shown in other organisms, but instead feel that either more efficient knockdowns or a total knockout would be needed to replicate the strong effect seen with Bud13 depletion.

With respect to Irf7, the fact that a crucial immunological gene has such an intron, with its variety of seemingly negative characteristics that make it difficult for the spliceosome to excise, begs the question as to why it exists. At the heart of an inflammatory response is a tightly regulated gene expression program. Regulation of this gene expression program is crucial as small changes can shift the balance away from protective immunity towards either nonexistent or destructive immunity.[33] Here we've shown that alterations to the splicing efficiency of the fourth intron have the ability to significantly alter the functional output of Irf7. Thus, by existing in the Irf7 transcript and commonly being retained, it stands to reason the weak fourth intron acts to dampen Irf7 output, perhaps as a means to mitigate what otherwise would be an unchecked or inappropriately scaled response. Whether a cell actively controls this splicing event and thus, the intron serves as a regulatory control point, remains unknown. Further, it remains unknown whether Bud13 plays a role in this regulation or whether it simply represents a mechanism that evolved to counter intron retention in a subset of introns that require splicing but happen to be inherently weak.

In summary, we found that Bud13 modulates gene expression through its ability to alter IR, often in notably small, GC-rich introns with weak splice sites. Deficiency of Bud13 results in IR and concomitant decreased gene expression in transcripts such as Irf7, dampening the type I interferon response and increasing viral susceptibility. Therefore Bud13, in mediating Irf7 gene expression, presents a potential therapeutic target for the treatment of infections or autoimmune conditions. Future studies should seek to understand why Bud13 is vital for the efficient splicing of only a subset

of junctions and whether or not this junction specificity plays an active role in regulating gene expression. If modulated, this strategy by which components associated with the spliceosome rescue transcripts from intron retention and degradation may represent a previously underappreciated layer of regulation in many gene expression programs.

ACKNOWLEDGEMENTS

The authors would like to thank Mario Blanco and Mitchell Guttman (Dept. of Biology, Caltech) for assistance with eCLIP analysis; Patricia Turpin, Mati Mann, Guideng Li, and Alok Joglekar (Dept. of Biology, California Institute of Technology) for experimental and computational assistance. Additionally, the authors would like to thank Genhong Cheng (Department of Microbiology, Immunology & Molecular Genetics, UCLA) for VSV and Jae Jung (Department of Molecular Microbiology & Immunology, USC) for VSV-GFP. This work was funded from a grant from NIH (5R21AI126344) and from an endowment provided by the Raymond and Beverly Sackler Foundation.

AUTHOR CONTRIBUTIONS

L.S.F, D.M., and D.B., conceived and designed experiments. L.S.F. conducted experiments. C.B. helped develop RAP-MS and knockdown experiments. L.S.F. and D.M. analyzed sequencing data. A.M. oversaw mass spectrometry and M.J.S. performed mass spectrometry analysis. L.S.F, D.M., and D.B wrote the manuscript with input from all authors.

References:

1. Schmitz, U. *et al.* Intron retention enhances gene regulatory complexity in vertebrates. *Genome Biol.* **18,** 216 (2017).
2. Wong, J. J.-L., Au, A. Y., Ritchie, W. & Rasko, J. E. Intron retention in mRNA: No longer nonsense. *Bioessays* **38,** 41–49 (2016).
3. Wong, J. J.-L. *et al.* Orchestrated intron retention regulates normal granulocyte differentiation. *Cell* **154,** 583–595 (2013).
4. Yap, K., Lim, Z. Q., Khandelia, P., Friedman, B. & Makeyev, E. V. Coordinated regulation of neuronal mRNA steady-state levels through developmentally controlled intron retention. *Genes Dev.* **26,** 1209–1223 (2012).
5. Dvinge, H. & Bradley, R. K. Widespread intron retention diversifies most cancer transcriptomes. *Genome Med.* **7,** 45 (2015).
6. Braunschweig, U. *et al.* Widespread intron retention in mammals functionally tunes transcriptomes. *Genome Res.* **24,** 1774–1786 (2014).
7. Honda, K. *et al.* IRF-7 is the master regulator of type-I interferon-dependent immune responses. *Nature* **434,** 772–777 (2005).
8. Ciancanelli, M. J. *et al.* Life-threatening influenza and impaired interferon amplification in human IRF7 deficiency. *Science* **348,** 448–453 (2015).
9. Harley, J. B. *et al.* Genome-wide association scan in women with systemic lupus erythematosus identifies susceptibility variants in ITGAM, PXK, KIAA1542 and other loci. *Nat. Genet.* **40,** 204 (2008).
10. Shalek, A. K. *et al.* Single-cell transcriptomics reveals bimodality in expression and splicing in immune cells. *Nature* **498,** 236 (2013).

11. McHugh, C. A. *et al.* The Xist lncRNA interacts directly with SHARP to silence transcription through HDAC3. *Nature* **521,** 232–236 (2015).
12. Yeo, G. & Burge, C. B. Maximum entropy modeling of short sequence motifs with applications to RNA splicing signals. *J. Comput. Biol.* **11,** 377–394 (2004).
13. Dziembowski, A. *et al.* Proteomic analysis identifies a new complex required for nuclear pre-mRNA retention and splicing. *EMBO J.* **23,** 4847–4856 (2004).
14. Jacob, A. G. & Smith, C. W. Intron retention as a component of regulated gene expression programs. *Hum. Genet.* 1–15 (2017).
15. Mostafavi, S. *et al.* Parsing the interferon transcriptional network and its disease associations. *Cell* **164,** 564–578 (2016).
16. Schneider, C. *et al.* Dynamic Contacts of U2, RES, Cwc25, Prp8 and Prp45 Proteins with the Pre-mRNA Branch-Site and 3' Splice Site during Catalytic Activation and Step 1 Catalysis in Yeast Spliceosomes. *PLOS Genet.* **11,** e1005539 (2015).
17. Consortium, E. P. An integrated encyclopedia of DNA elements in the human genome. *Nature* **489,** 57–74 (2012).
18. Lund, J. M. *et al.* Recognition of single-stranded RNA viruses by Toll-like receptor 7. *Proc. Natl. Acad. Sci. U. S. A.* **101,** 5598–5603 (2004).
19. Sayani, S. & Chanfreau, G. F. Sequential RNA degradation pathways provide a fail-safe mechanism to limit the accumulation of unspliced transcripts in Saccharomyces cerevisiae. *Rna* **18,** 1563–1572 (2012).
20. Na, I., Meng, F., Kurgan, L. & Uversky, V. N. Autophagy-related intrinsically disordered proteins in intra-nuclear compartments. *Mol. Biosyst.* **12,** 2798–2817 (2016).

518 21. Zhou, Y. & Johansson, M. J. The pre-mRNA retention and splicing complex controls
519 expression of the Mediator subunit Med20. *RNA Biol.* 1–7 (2017).
520 22. Zhou, Y., Chen, C. & Johansson, M. J. The pre-mRNA retention and splicing complex
521 controls tRNA maturation by promoting TAN1 expression. *Nucleic Acids Res.* **41,** 5669–
522 5678 (2013).
523 23. Ni, L. & Snyder, M. A Genomic Study of the Bipolar Bud Site Selection Pattern
524 inSaccharomyces cerevisiae. *Mol. Biol. Cell* **12,** 2147–2170 (2001).
525 24. Bao, P., Will, C. L., Urlaub, H., Boon, K.-L. & Lührmann, R. The RES complex is required
526 for efficient transformation of the precatalytic B spliceosome into an activated Bact complex.
527 *Genes Dev.* (2018).
528 25. Ohrt, T. *et al.* Prp2-mediated protein rearrangements at the catalytic core of the spliceosome
529 as revealed by dcFCCS. *RNA* **18,** 1244–1256 (2012).
530 26. Fabrizio, P. *et al.* The evolutionarily conserved core design of the catalytic activation step of
531 the yeast spliceosome. *Mol. Cell* **36,** 593–608 (2009).
532 27. Plaschka, C., Lin, P.-C. & Nagai, K. Structure of a pre-catalytic spliceosome. *Nature* **546,**
533 617 (2017).
534 28. Bertram, K. *et al.* Cryo-EM structure of a pre-catalytic human spliceosome primed for
535 activation. *Cell* **170,** 701–713 (2017).
536 29. Blanco, M. R. *et al.* Single Molecule Cluster Analysis dissects splicing pathway
537 conformational dynamics. *Nat. Methods* **12,** 1077 (2015).
538 30. Hoskins, A. A. & Moore, M. J. The spliceosome: a flexible, reversible macromolecular
539 machine. *Trends Biochem. Sci.* **37,** 179–188 (2012).

31. Fernandez, J. P. *et al.* RES complex is associated with intron definition and required for zebrafish early embryogenesis. *PLoS Genet.* **14,** e1007473 (2018).

32. Jiang, M. *et al.* Genome-wide analysis of developmental and sex-regulated gene expression profiles in Caenorhabditis elegans. *Proc. Natl. Acad. Sci.* **98,** 218–223 (2001).

33. Kontoyiannis, D., Pasparakis, M., Pizarro, T. T., Cominelli, F. & Kollias, G. Impaired on/off regulation of TNF biosynthesis in mice lacking TNF AU-rich elements: implications for joint and gut-associated immunopathologies. *Immunity* **10,** 387–398 (1999).

34. Liu, J. M., Sweredoski, M. J. & Hess, S. Improved 6-Plex Tandem Mass Tags Quantification Throughput Using a Linear Ion Trap–High-Energy Collision Induced Dissociation MS3 Scan. *Anal. Chem.* **88,** 7471–7475 (2016).

35. Kim, D. *et al.* TopHat2: accurate alignment of transcriptomes in the presence of insertions, deletions and gene fusions. *Genome Biol.* **14,** R36 (2013).

36. Trapnell, C. *et al.* Transcript assembly and quantification by RNA-Seq reveals unannotated transcripts and isoform switching during cell differentiation. *Nat. Biotechnol.* **28,** 511–515 (2010).

37. Anders, S., Pyl, P. T. & Huber, W. HTSeq—a Python framework to work with high-throughput sequencing data. *Bioinformatics* **31,** 166–169 (2015).

38. Shen, S. *et al.* rMATS: robust and flexible detection of differential alternative splicing from replicate RNA-Seq data. *Proc. Natl. Acad. Sci.* **111,** E5593–E5601 (2014).

39. Corvelo, A., Hallegger, M., Smith, C. W. & Eyras, E. Genome-wide association between branch point properties and alternative splicing. *PLoS Comput. Biol.* **6,** e1001016 (2010).

40. Van Nostrand, E. L. *et al.* Robust transcriptome-wide discovery of RNA-binding protein binding sites with enhanced CLIP (eCLIP). *Nat. Methods* **13,** 508–514 (2016).

41. Shen, L., Shao, N., Liu, X. & Nestler, E. ngs. plot: Quick mining and visualization of next-generation sequencing data by integrating genomic databases. *BMC Genomics* **15,** 284 (2014).

42. Lovci, M. T. *et al.* Rbfox proteins regulate alternative mRNA splicing through evolutionarily conserved RNA bridges. *Nat. Struct. Mol. Biol.* **20,** 1434–1442 (2013).

43. Budak, G., Srivastava, R. & Janga, S. C. Seten: a tool for systematic identification and comparison of processes, phenotypes, and diseases associated with RNA-binding proteins from condition-specific CLIP-seq profiles. *RNA* **23,** 836–846 (2017).

FIGURE LEGENDS

Figure 1: *Irf7* contains a weak intron that is following many forms of stimulation. (A) Histogram of mapped reads corresponding to the TNFα-induced expression of Irf7. The poorly spliced fourth intron is highlighted. For all read density plots, reads are histogrammed in $\log_{10}$ scale and normalized to the maximum value across the stimulation. **(B)** Comparison of Irf7 splice donor and acceptor sites in mice, rats, and humans. **(C-F)** Histogram representing the intron length **(C),** intron GC content **(D)**, flanking exon GC content **(E)**, or 5' splice site strength of introns of expressed in BMDMs. Red represents location of Irf7 intron 4 **(C, D, F)** or upstream exon **(E)**. Black line represents downstream exon **(E)**. **(G, H)** Histogram of mapped reads corresponding to the IFNα **(G)** and poly(I:C) **(H)** induced expression of Irf7 focused on the slow splicing fourth intron. **(I)** Outline of Splicing Ratio (SR) metric. **(J)** Splicing ratio for all introns in Irf7 plotted against time stimulated with TNFα.

Figure 2: RAP-MS and RIP identifies Bud13 as an RNA binding protein that interacts with IRF7 mRNA. (A) Outline of the RAP-MS procedure used to identify RNA-binding proteins on transcritps of interest. **(B)** TMT ratio (Irf7/Actb) for proteins identified as enriched on either Irf7 (TMT ratio >1) or Actb (TMT ratio <1) transcripts. **(C)** RT-qPCR analysis of transcripts captured via RAP for Irf7 (blue) and Actb (gold) probes. **(D)** RIP followed by RT-qPCR for Irf7 and Rpl32 in TNFα stimulated BMDMs. Shown is the relative enrichment of transcripts captured in Bud13 RIP as compared to Rabbit IgG RIP. **(E)** Same as (d) except stimulation with poly(I:C). Data are representative of two independent experiments ((**C-E),** mean + SEM). *P < 0.05, **P < 0.01 and ***P < 0.001 (t-test).

Figure 3: Bud13 knockdown leads to increased retention in the poorly splicing intron of Irf7. (A) Histogram of mapped reads corresponding to the TNFα-induced expression of Irf7. The poorly spliced fourth intron is highlighted. shBud13 samples are shown in green. Control samples are shown in grey. **(B)** ΔSRs calculated for each junction in the Irf7 transcript. The ΔSR of intron 4 as compared to all other junctions is significant (Student's t-test, p<0.001). No other pairwise comparison is significant. **(C)** Splicing gel from RNA extracted from BMDMS stimulated for 30 mins. TNFα (top). Quantification of splicing gel (bottom). **(D)** Irf7 FPKM fold change with respect to time stimulated. shBud13 is shown in green, control is shown in grey. Data is representative of two independent experiments **(C)** and is represented as mean + SEM. * denotes p < 0.05, ** denotes p < 0.01, and *** denotes p < 0.001 using a Student's t test.

Figure 4: Bud13 knockdown alters the type I interferon response. (A) Histogram of mapped reads corresponding to the TNFα-induced expression of Irf7. The poorly spliced fourth intron is highlighted. shBud13 samples are shown in blue. Control samples are shown in grey. **(B)** ΔSRs calculated for each junction in the Irf7 transcript. The ΔSR of intron 4 as compared to all other junctions is significant (Student's t-test, p<0.001). No other pairwise comparison is significant. **(C)** Irf7 FPKM fold change with respect to time stimulated. shBud13 is shown in blue, control is shown in grey. **(D) I**mmunoblot analysis of Irf7 protein following 720 mins. poly(I:C) stimulation (left). Quantification relative to ActB (right). **(E)** Log_2 expression fold change (shBud13/control) for 119 ISGs in unstimulated BMDMs (median = 0.1655). **(F)** As in **(E)** for stimulated BMDMs (720 mins poly(I:C) (median = -0.1007). Wilcoxon rank-sum between **(E)** and **(F)**, *P*< .001. **(G)** Median $\log_2$ expression fold change (shBud13/control) for ISGs in unstimulated BMDMs, and BMDMs stimulated with Poly(I:C) 15, 60, 240, 720, and 1440 mins. Bars represent 95% CI. (Wilcoxon rank-sum, *P*< .001, for any of the 'early' time-points (0, 15, 60 mins) compared to any of the 'late' time-points (240, 720, 1440 mins). **(H)** RT-qPCR analysis of IFNα mRNA levels in unstimulated BMDMs and BMDMs stimulated with poly(I:C) for 720 mins and 1440 mins. **(I)** Same as **(H)** for IFNβ. **(J)** Nuclear fraction (top) and cytoplasmic fraction (bottom) histograms of mapped reads corresponding to the poly(I:C)-induced expression of Irf7 (720 mins). The poorly spliced fourth intron is highlighted. shBud13 samples are shown in blue. Control samples are shown in grey. Nuclear ΔSR = 0.35. **(K)** Nuclear and cytoplasmic RPKM for Irf7 intron 4 from fractionated BMDMs stimulated with poly(I:C). **(L)** Cytoplasmic Irf7 FPKM for control (grey) and shBud13 BMDMs stimulated with poly(I:C). Data is representative of four independent experiments **(H, I)** and is represented as mean + SEM. * denotes p < 0.05, ** denotes p < 0.01, and *** denotes p < 0.001 using a Student's t test. Results are presented relative to those of Rpl32 **(H,I).**

Figure 5: Global analysis of the role of Bud13. (**A)** Ranked bar chart showing genes with a junction most affected by Bud13 knock-down in all samples during TNFα stimulation. See S7 for histograms relating to most affected junctions. (**B)** Grouped bar chart depicting the number of genes that have a single Bud13 affected junction vs. multiple Bud13 affected junctions using three different ΔSR thresholds. **(C)** Transcripts were classified as 'Bud13 dependent' if they had a junction with a ΔSR. >0.15. The $\log_2$ expression fold change (FPKM shBud13/ FPKM control) for each gene represented by the transcripts in the 'Bud13 dependent' category as well as all other genes is shown. Median 'increased IR' = -0.5084. Median 'decreased IR' = -0.2170. (Wilcoxon rank-sum, $P < .01$). **(D)** Mean ΔSR. for junctions below the indicated threshold (x-axis) vs. mean ΔSR. for all junctions. Threshold applied for the 5' splice site (blue) and the 3' splice site (green). **(E)** 5'SS motif for all expressed junctions as compared to junctions that show retention upon Bud13 knockdown (ΔSR. > 0.15). **(F)** Size of intron for introns retained upon Bud13 knockdown (ΔSR. > 0.15) (blue), in introns located in the same transcript as those affected by Bud13 (green), and in introns from all expressed transcripts (orange). **(G)** Same as **(F)** for GC content. **(H)** Flanking exon GC content for exons that flank introns retained upon Bud13 knockdown (ΔSR. > 0.15) (dark green) as compared to exons that flank introns from all expressed transcripts (light green). **(I)** Distance from the branch point to the 3' splice site for introns retained upon Bud13 knockdown (ΔSR. > 0.15) (dark blue) as compared to introns from all expressed transcripts (light blue). **(F-I)** data from BMDM TNFα stimulation. Box plots show median (center line), interquartile range (box) and tenth and ninetieth percentiles. $*P < 0.05$, $**P < 0.01$ and $***P < 0.001$ (Mann-Whitney *U*-test).

Figure 6: Bud13 interacts primarily near the 3' splice site of small, GC rich introns. (A) eCLIP-seq read density plots in K562 cells. Bud13 density plot over all expressed junctions shown in blue (top), Bud13 density plot over Bud13 dependent junctions shown in red (top). Sf3b4 density plot over all expressed junctions shown in maroon (middle), and Prpf8 density plot over all expressed junctions is shown in green (bottom). **(B)** Same as in **(A)** but for Hep G2 cells. **(C)** Bud13 eCLIP-seq peak distribution. Peaks fell within either intronic regions, intron-exon junctions, or exonic regions. Peaks that fell within intron-exon junction were further classified as 5' junction peaks or 3' junction peaks (bottom). **(D)** Same as **(C)** but for Hep G2. **(E)** Size of all introns in expressed transcripts for the given cell line (dark blue) vs size of introns with overlapping eCLIP peak (maroon). Shown in K562 (left) and Hep G2 (right) cells. Box plots show median (center line), interquartile range (box) and tenth and ninetieth percentiles (whiskers). $*P < 0.05$, $**P < 0.01$ and $***P < 0.001$ (Mann-Whitney *U*-test). **(F)** Same as **(E)** for GC content. **(G)** GO terms (biological process) enriched among Bud13 eCLIP peaks in K562(dark blue) and Hep G2 (maroon) cells.

Figure 7: Bud13 knockdown alters the BMDM response to VSV. (A) RT-qPCR analysis of Irf7 mRNA levels in infected control or shBud13 BMDMs stimulated with VSV (MOI 5) across 24 hours. **(B)** Same as in **(A)** except stimulated at an MOI of 10. Results are presented relative to those of Rpl32. **(C)** PFU/mL for viral supernatant from infected shBud13 (blue), control (red), shBud13 with Irf7 overexpression (yellow), or control with Irf7 overexpression (maroon) BMDMs. Data is representative of two **(A, B)** or three independent experiments **(C)** and is shown as mean + SEM. * denotes $p < 0.05$, ** denotes $p < 0.01$, and *** denotes $p < 0.001$ using a Student's t test

STAR METHODS

Contact for Reagent and Resource Sharing

Further information and requests for resources and reagents should be directed to and will be fulfilled by the Lead Contact, David Baltimore (baltimo@caltech.edu).

Experimental Model and Subject Detail

Animals

The California Institute of Technology Institutional Animal Care and Use Committee approved all experiments. C57BL/6 WT mice were bred and housed in the Caltech Office of Laboratory Animal Resources (OLAR) facility. C56BL6/J mice were sacrificed via CO2 euthanasia and sterilized with 70% ethanol. Femur and tibia bones harvested and stripped of muscle tissue. Bone marrow cells were resuspended in 20mL of fresh DMEM. 2.5 *10^6 bone-marrow cells plated in a 150mm dish in 20mL of BMDM Media (DMEM, 20% FBS, 30% L929 condition media, and 1% Pen/Strep) and grown at 5% CO_2 and 37°C. BMDM media was completely replaced on day 3 as well as a supplemental addition of 5mL L929 condition media on day 5.

Cell Culture

Human embryonic kindey cells (HEK293T) from ATCC were cultured in DMEM supplemented with 10% FBS and 1% Pen/Strep. Cell line was maintened at 37°C in 5% CO_2.

Method Detail

Knockdown Experiments

BMDMs for knockdown experiments were grown as described above with a few additions. On days 3 and 4, retrovirus encoding shRNAs were added to cells. On day 5, cells were selected with puromycin (5ug/mL). On day 8, following ~72 hours of puromycin treatment, media was removed and 10mL of PBS w/ 2mM EDTA was added. Cells were lightly scraped and replated in either 6 well plates or 10-cm dishes depending on the experiment. Cells were left in BMDM media overnight. The following day, cells were stimulated with either 20ng/mL of TNFα, 5ug/mL Poly(I:C) (Sigma), or ODN 1585 (1-5 μM) (InvivoGen).

RNA Isolation:

Total RNA was purified from BMDMs using TRIzol reagent (Ambion) as per the manufacturer's instructions. Genomic DNA in RNA purifications was eliminated through treatment with Turbo DNase (Thermo Fisher Scientific) for 30 min at 37°C. 0.1-1μg RNA and 1μM dT(30) oligo (d14-954: 5'-AAGCAGTGGTATCAACGCAGAGTACT(30)) was heated at 80°C for 2.5min followed by snap cooling on ice. 10μL template-switch RT mix added (10μM template-switch oligo (TSO: 5'-AAGCAGTGGTATCAACGCAGAGTACACArGrGrG), 20mM DTT, 2X ProtoScriipt II Reverse Transcriptase Reaction Buffer (NEB), 1mM dNTPs, 40U Murine RNAse Inhibitor (NEB), and 200U ProtoScript II (NEB) Reverse Transcriptase. Reaction incubated in thermocycler with the following program: 1. 42°C for 30min, 2. 45°C for 30min, 3. 50°C for 10min, followed by deactivation of RT for 10min at 80°C.

RNA Fractionation:

Confluent 10-cm dish of mature BMDMs were scraped into 400μL cold NP-40 lysis buffer, APJ1 (10mM Tris-HCl (pH 7.5), 0.08% NP-40, 150mM NaCl). Lysed cells layered onto 1mL cold sucrose 322 cushion, APJ2 (10mM Tris-HCl (pH 7.5), 150mM NaCl, 24% w/v sucrose) and centrifuged for 10min at 4°C and 13000 rpm. The supernatant from this spin represents the cytoplasmic RNA fraction, which is immediately added to 3 volumes of 100% ethanol and 2 volumes of buffer RLT (4M GuSCN, 325 0.1M β-mercaptoethanol, 0.5% N-lauroyl sarcosine, 25mM Na-citrate, pH7.2) and

stored at -80°C until ready to purify RNA. Pellet, containing intact nuclei, is resuspended in 500µL TRIzol reagent. If the pellet was difficult to dissolve, it was heated at 50°C with occasional vortexing. 100µL chloroform added and shaken vigorously for 15-20s; allowed to phase separate at room temperature for 5min. Tube centrifuged at 4°C and 12000 x g for 15min. Clear upper aqueous phase removed to a new tube, ensuring white DNA mid-phase is not removed, and is immediately added to 3 volumes of 100% ethanol and 2 volumes of buffer RLT and stored at -80°C until ready to purify RNA. RNA is purified according to Qiagen RNeasy column protocol and eluted in 30µL nuclease-free H2O. RNA samples are DNAse treated with Turbo-DNAse and stored at -80°C.

Library preparation and RNA-Seq Analysis

Limited PCR amplifications was performed prior to library preparation. PCR reaction done with KAPA HiFi HotStart 2x ReadyMix, 5% cDNA, and 1µM primer (d14-955: 5'-AAGCAGTGGTATCAACGCAGAGTACT). Thermal cycler programmed for 120 seconds at 95°C as initial denaturation, followed by 14 cycles of 30sec at 95°C for denaturation, 30sec at 62.5°C as annealing, 150sec at 72°C for extension, and final extension at 72°C for 5 min. PCR reactions 0.9X SeraMag and eluted in 25µL. Concentrations of purified library determined using Qubit High Sensitivity dsDNA kit (Invitrogen) as described. Full length cDNA libraries were barcoded using the Nextera XT Tagmentation protocol (Illumina).

RNA-Antisense Purification

RNA antisense purification-mass spectrometry (RAP-MS) was performed as described in McHugh et al. with a few alterations. Briefly, we designed three 90-mer DNA oligonucleotide probes that were antisense to the complementary target RNA sequence in both *Irf7* and *Actb* transcripts. Each probe was targeted to a different location on the transcript and modified with a biotin in order to enable capture of DNA:RNA hybrids on streptavidin coated magnetic beads.

RNA Prep and Lysis: ~250million cells, or 25 150mm plates of BMDMs were used for each capture. Following stimulation with TNFα (20ng/ml) for 30 minutes, ~5-10 mL of PBS w/ 2mM EDTA was added to each plate and cells were removed by lightly scraping. Cells were pelleted, resuspended in PBS, and poured into a new 150mm plate. The cells were then crosslinked in Spectrolinker at 254 nm wavelength with 0.8 J/cm2 (instrument setting: 8000 x 100 uJ/cm^2). Following crosslinking, cells were again pelleted, at which point the pellet could be frozen and stored at -80°C. Cells were lysed in 2mL of lysis buffer per capture (10 mM Tris pH 7.5, 500 mM LiCl, 0.5% Triton X-100, 0.2% sodium dodecyl sulphate, 0.1% sodium deoxycholate) supplemented with Protease Inhibitor Cocktail (EMD Millipore) and 1000 U of Murine RNase Inhibitor (New England Biolabs). We found the smaller the volume used per sample, the more efficient the capture was downstream and thus the minimum volume needed to lyse cells should be optimized. Samples were incubated for 10 min on ice to allow lysis. Following lysis, sample was passed through 20-gauge needle once and then 26-gauge needle 3-5 times to disrupt the pellet and shear genomic DNA. In between passing the sample through the 26-gauge needle, the sample was sonicated on ice with a microtip set at 5W power for a total of 30 s in intermittent pulses (0.7 s on, 1.3 s off). Samples were then mixed with twice the lysate volume of 1.5x LiCl/Urea Buffer (the final buffer contains 10 mM Tris pH 7.5, 500 mM LiCl, 0.5% Triton X-100, 0.2% SDS, 0.1% deoxycholate, 4 M urea). Lysates were incubated on ice for 10 min then cleared by centrifugation for 10 min at 4,000g.

Pre-clearing lysate: BioMag streptavidin beads (Bang Laboratories Inc.) were first washed 3x in 0.25-0.5ml of 500mM LiCl/4M Urea buffer (10 mM Tris pH 7.5, 500 mM LiCl, 0.5% Triton X-100, 0.2% SDS, 0.1% deoxycholate, 4 M urea). 50ul of beads were added to each sample and the samples were incubated at 37°C for 30 min with shaking. Streptavidin beads were then magnetically separated from lysate samples using a magnet. The beads used for preclearing lysate were discarded and the lysate sample was transferred to fresh tubes twice to remove all traces of magnetic beads. Input for quality control experiments can be removed at this point.

Hybridization, Capture of Probes and Elution of Associated Protein: Following pre-clearing, the biotinylated 90-mer DNA oligonucleotide probes specific for the RNA target of interest (vary per sample but ~5ul of 25uM per probe) were heat-denatured at 85°C for 3 min and then snap-cooled on

ice. Probes and pre-cleared lysate were mixed and incubated at 55°C with shaking for 2 h to hybridize probes to the capture target RNA. 500mL of washed streptavidin beads (Bang Laboratories Inc.) were then added to each sample at 55°C with shaking for 30 mins. Beads with captured hybrids were washed 6 times with LiCl/Urea Hybridization Buffer. If needed, 1% of the beads can be removed for qPCR quality control experiment. TRIzol reagent can be added directly to beads to elute RNA. Beads were then resuspended in Benzonase Elution Buffer (20 mM Tris pH 8.0, 2 mM MgCl2, 0.05% NLS, 0.5 mM TCEP) and 125 U of Benzonase nonspecific RNA/DNA nuclease was added. Incubation occurred for 1-2 h at 37°C. Beads were then separated from the sample using a magnet. Supernatant was collected. Contaminant beads were removed by 5 rounds of magnetic separation on supernatant. Protein was precipitated overnight at 4°C with 10% trichloroacetic acid (TCA). TCA treated protein elution samples were pelleted by centrifugation for 30 min at 20,000g, then washed with 1 ml cold acetone and recentrifuged. Final protein elution pellets were air dried to remove acetone, resuspended in fresh 8 M urea dissolved in 40 ml of 100 mM Tris-HCl pH 8.5, and stored at -20°C.

Mass Spec Prep. and Analysis Performed as in McHugh et al. with few exceptions. Instead of SILAC we label proteins at the mass spec prep step using TMT (Thermo). After desalting on a Microm Bioresources C8 peptide MicroTrap column and lyophilization of peptide fraction, lyophilized protein pellets were resuspended in 100mM TEAB at a concentration of 1ug/ul. We then added 1.64ul of TMT labelling reagent to each ug of sample. The reaction was incubated for one hour at room temperature. The reaction was quenched with 0.32ul of 5% hydroxylamine per ug of protein used and incubated for 15 mins at room temperature. Following quenching, the samples were mixed, desalted as before, lyophilized, and mass spec was performed on Orbitrap Fusion mass spectrometer using a TMT instrument method as described in Liu et al.[34]

Raw files were searched using MaxQuant (v. 1.5.3.30) against the UniProt mouse database (59550 sequences) and a contaminant database (248 sequences). TMT 6plex was selected as the quantitation method with a reporter mass tolerance of 0.3. Oxidation of methionine and protein N-terminal acetylation were variable modifications and carbamidomethylation of cysteine was fixed modification. A 1% protein and peptide false discovery rate as estimated by the target-decoy approach was used for identification.

RNA Immunoprecipitation

RNA immunoprecipitations were performed as previously described. Between 5-10 confluent 15 cm^2 dishes of BMDMs per sample were stimulated with either 20ng/mL of TNFα for 30 minutes or 5ug/mL Poly(I:C) for 12 hours. Following stimulation, proteins were cross-linked to DNA by adding formaldehyde directly to the media to a final concentration of 0.75%, with light shaking at room temperature for 10 mins. To quench the crosslinking reaction, glycine to a final concentration of 125 mM was added to the media and incubated with shaking for 5 mins at room temp. Media was then aspirated and cells were rinsed twice with 10 mL of cold PBS. Following the second wash, cells were scraped into 10mL of PBS and spun down gently (5 min, 4°C, 1,000xg). Final cell pellet was resuspended in 0.1-1mL of polysome lysis buffer (100 mM KCl, 5 mM $MgCl_2$, 10 mM HEPES (pH 7.0), 0.5% NP40, 1 mM DTT, 100 U.ml RNase Inhibitor (NEB)) supplemented with Protease Inhibitor Cocktail (EMD Millipore). At this point the mRNP lysate was frozen. If needed, passing the lysate through a small gauge needle can help with lysate. Protein-G beads were pre-treated at 4°C with NT2 (50 mM Tris-HCl (pH 7.4), 150 mM NaCl, 1 mM $MgCl_2$, 0.05% NP40) supplemented with 5% BSA to a final ratio of 1:5 for at least 1h before use. Appropriate amount of antibody per sample (optimized based on antibodyused but typically ~1-10ug) was added ot 250-500ul of bead/BSA slurry and incubated at 4°C. Following incubation, beads were spun down and washed with 1 ml of ice-cold NT2 buffer 4–5 times. Following final wash, beads were resuspended in 850ul of NT2 and supplemented with 200U of RNase inhibitor, 10 µl of 100 mM DTT and EDTA to 20 mM. Frozen lysate was thawed and centrifuged at 15,000*g for 15 mins. The cleared supernatant was removed and 100ul was added to the prepared beads. Input removed at this step. Beads and lysate were incubated for 4h at 4°C with mixing. The beads were washed 4-5 times with ice-cold NT2 and then resuspended in 100ul of NT2 buffer. 4ul of 5M NaCl was added incubated with shaking at 65°C for 2

hours. NT2 buffer can also be supplemented with 30 µg of proteinase K to release the RNP component. RNA was isolated by adding TRIzol reagent (Ambion) as per the manufacturer's instructions. RNA was reverse transcribed and quantification was performed using TaqMan qPCR.

Immunoblot

BMDM samples were prepared as described previously. On day 8, they were plated at similar density. Following adherence, BMDMs were stimulated with Poly(I:C) or CpG for the indicated time. Cells were scraped into subcellular fractionation buffer (20mM HEPES (pH 7.4), 10 mM KCl, 2 mM $MgCl_2$, 1mM EDTA, 1 mM EGTA). The cells were then passed through a 27 gauge needle 10 times, incubated on ice for 10 mins, and spun down at 720xg for 5 min. The pellet contained the nuclei, which was washed with fractionation buffer, passed through a 25 gauge needle 10 times, and centrifuged again at 720xg for 10 mins. The resulting pellet was resuspended in RIPA lysis buffer. Queal amounts of proteins were analyzed by immunoblot using the following reagents: anti-IRF7 (Millipore, ABF130), anti-Lamin B1 HRP conjugate (Cell Signalling, D9V6H), and anti-rabbit IgG HRP conjugate (Cell Signalling).

Viral Plaque Assays

Plaque assays were done one Vero cells. $2.5*10^5$ vero cells were plated in a 12 well plate the night before infection. Prior to infection, cells were checked to ensure confluence. VSV was serially diluted and infected in 12 well plate for 1 h. VSV was then removed and cells were layered carefully with DMEM supplemented with 2% FBS and 0.4% agarose. Plate was incubated for 2 days, and then fixed with 10% formaldehyde, for 1 h to overnight. Finally, agarose plugs were removed carefully and cells were stained with crystal violet.

VSV-GFP Infection Experiment

BMDMs were grown as described above in 150mm dishes. On day 8, following ~72 hours of puromycin treatment, media was removed and 10mL of PBS w/ 2mM EDTA was added. Cells were lightly scraped and 250,000 cells/well were replated in 12 well plates in BMDM media. Cells were left for 12 hours to adhere. Following adherence, VSV-GFP was added at the specified MOI for the specified amount of time. Following the time-course, cells were lightly scraped, washed and spun down, and resuspended in PBS. Samples were analyzed on a MACSQuant10 Flow Cytometry machine (Miltenyi). Gating strategy depicted in Fig. 7.

VSV-GFP Viral Supernatant Experiment

BMDMs were grown as described above in 150mm dishes. On day 8, following ~72 hours of puromycin treatment, media was removed and 10mL of PBS w/ 2mM EDTA was added. Cells were lightly scraped and 400,000 cells/well were replated in 12 well plates in BMDM media. Cells were left to adhere for 12 hours, before being infected at an MOI of 25 for 8 hours. Following infection, virus was removed and the cells were washed with PBS three times. Then, 500ul of BMDM media (DMEM, 20% FBS, 30% L929 condition media, and 1% Pen/Strep) was added to each well. 18 hours later, media was collected and stored at -80°C. To titer viral supernatant, Vero cells were plated in a 96-well plate at 30,000 cells per well in 90ul of D10 media. 12 hours after plating, 90ul supernatant was added to the 90ul of D10 at different dilutions. PFU/mL was calculated from a standard curve with a virus of known concentration.

Quantification and Statistical Analysis

All statistical analysis was performed in Python (version 2.7.9). Unless otherwise indicated in figure legends, statistical significance measurements were marked as follows: * denotes $p < 0.05$, ** denotes $p < 0.01$, *** denotes $p < 0.001$, and n.s. denotes not significant. RNA-Seq expression and splicing analysis as well as eCLIP analysis is described in more detail below.

RNA-Sequencing Analysis

Sequencing was performed on a HiSeq 2500 High Throughput Sequencer (Illumina). Single-end 50-mer reads were aligned using Tophat v2.1.1.[35] Gene expression was determined using Cufflinks v2.2.1 and the FPKM (Fragments Per Kilobase Million) metric.[36]

Splicing Ratio and ΔSR Calculation

A custom script was written in Python using the HTSeq[37] library to calculate Splicing Ratio. First, reads that map to an intron or exon feature are summed. To map to a feature, reads must have >1 bp overlap with the feature. If a read maps to more than one feature, such as in the case of a splice junction read, the read is split between the features. SR is calculated by taking the length normalized number of reads that map to each intron, divided by the average length normalized number of exon reads plus the length normalized intron value. When SR is equal to 0, this indicates a junction is completely spliced. In contrast, large SR values indicate intron retention.
We use the SR value to calculate ΔSR, which is equal to SR(shBud13) – SR(Ctl). Values greater than 0 indicate the junction is more unspliced in the shBud13 sample, whereas values less than 0 indicate the junction is more unspliced in the Ctl sample. For the global analysis, in order for the ΔSR of a junction to be considered, it must pass through a number of filters. To account for transcripts that are annotated in Ensembl version 67, but not expressed, we set an FPKM threshold of 15. Further, a local normalized read count threshold on the upstream/downstream exons was implemented to ensure a level of sequencing depth needed to get accurate splicing values. To pass this threshold, the sum of the reads that map to the the upstream/downstream exons divided by the length of these exons must be ≥ 0.25.

ISG and Genome-Wide Analysis

ISGs used in Fig. 4 E-H were selected based on induction 2 hours after *in vivo* IFNa injection.[15] We classified ISGs to be any gene with a fold change ≥ 3.5 following 2 hours of induction. Intron RPKM was calculated using a custom python script with the HTSeq library. In Fig. 5a, transcripts from the 30 min. TNFα data-set that had a junction with a ΔSR value above 0.15 were sorted into an 'increased IR' category (ΔSR >0.15), whereas all other transcripts were sorted into an unaffected category (ΔSR <-0.15). The selected data-set is representative of all time-points from the TNFα, Poly(I:C) and CpG datasets. A maximum entropy model was used to calculate 3' and 5' splice site strengths.[12] To determine differences in 5' splice site sequence for Bud13 dependent junctions, the nine base pair sequence near the 5' splice site junctions for junctions that had a ΔSR >0.15 was compared to all expressed junctions (FPKM>1). The top Bud13 dependent junctions were plotted based on the average ΔSR value across all time-points from the TNFα data-set (Fig. 5D) as well as the Poly (I:C) data-set (Fig. SH). Junctions that had a ΔSR value <0.15 in a time-point were filtered out in the TNFα data-set, while junctions that had a ΔSR value <0.15 in two time-points were filtered out in the Poly (I:C) data-set. The zero time-point was removd for the transcripts induced by the stimulant (Irf7 and Cd14). For the comparison of alternative splicing events, rMATs[38] was used on the TNFα data-set. Splicing events were deemed significant if p<0.05 and FDR<0.1 for all time-points. SVMBPfinder was used to determine BP related features (BP strength and distance from BP to 3' splice site).[39]

eCLIP

Data for eCLIP experiments were downloaded from ENCODE Project Consortium.[18] Analysis of eCLIP data is the same as has been described previously.[40] Fold change of eCLIP read density compared to input read density along a normalized intron was calculated using ngs.plot.[41] Peaks were called using CLIPper.[42] Peaks were deemed significant if they were >3-fold enriched and had p-value<10^{-5}. Peak locations were determined using a custom python script with the HTSeq library. Enriched GO terms were determined using Seten.[43]

Data and Software Availability

The next-generation sequencing data reported in this study will be deposited to the Gene Expression Omnibus (GEO). Upon completion of deposit, the accession number for this data will be provided.

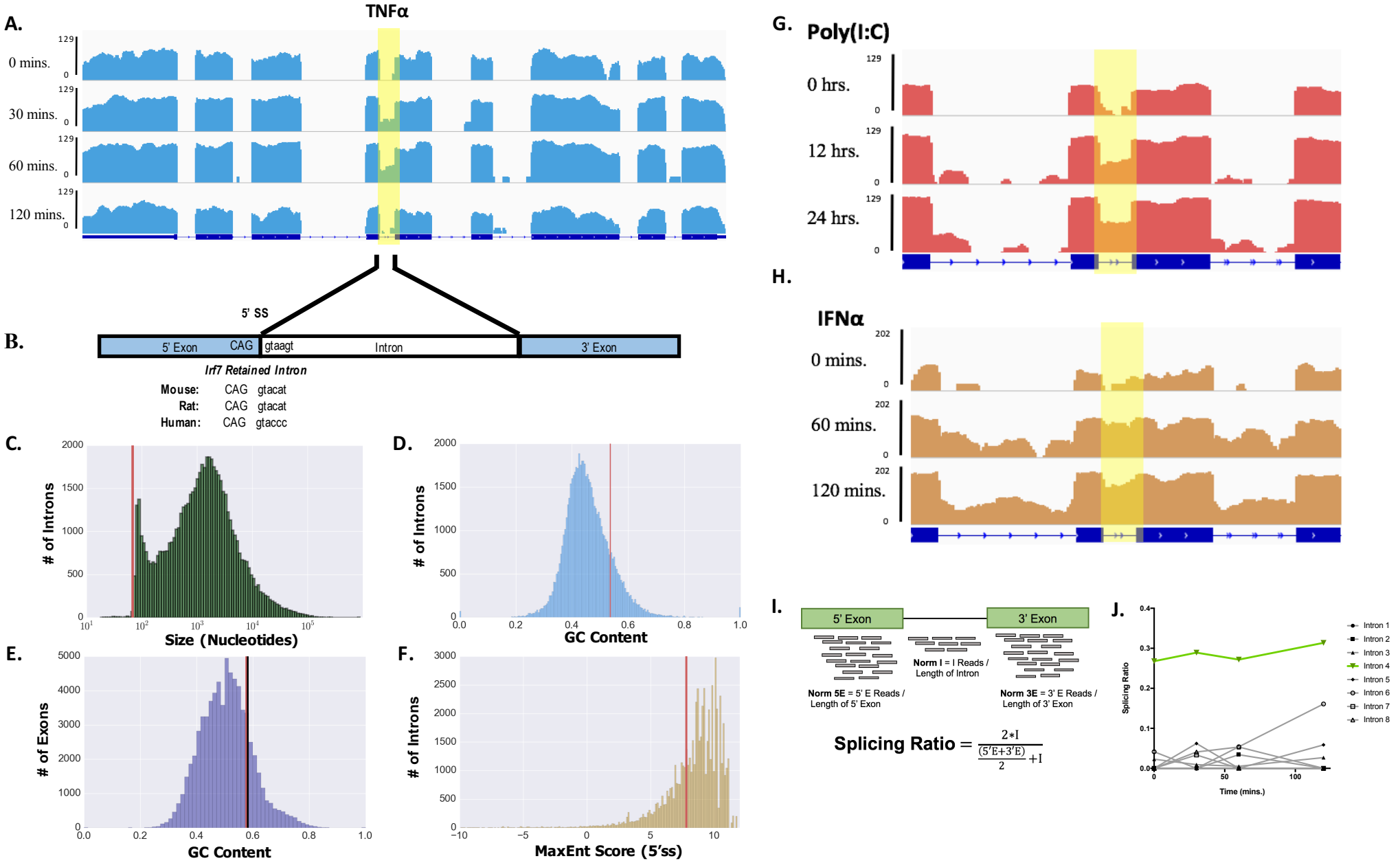

Figure 1: *Irf7* contains a weak intron that is retained following many forms of stimulation.

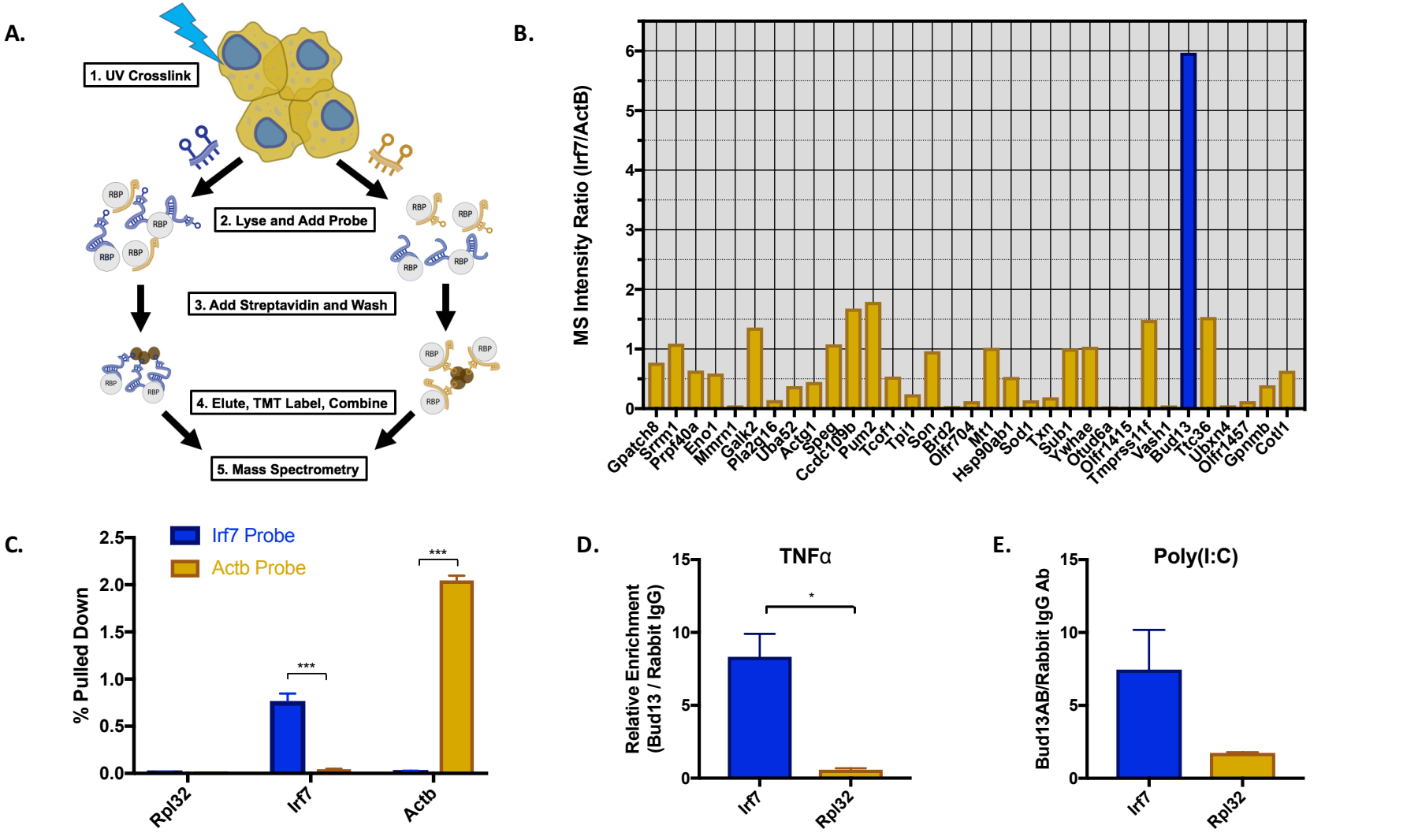

Figure 2: RAP-MS and RIP identify Bud13 as an RNA binding protein that interacts with IRF7 mRNA

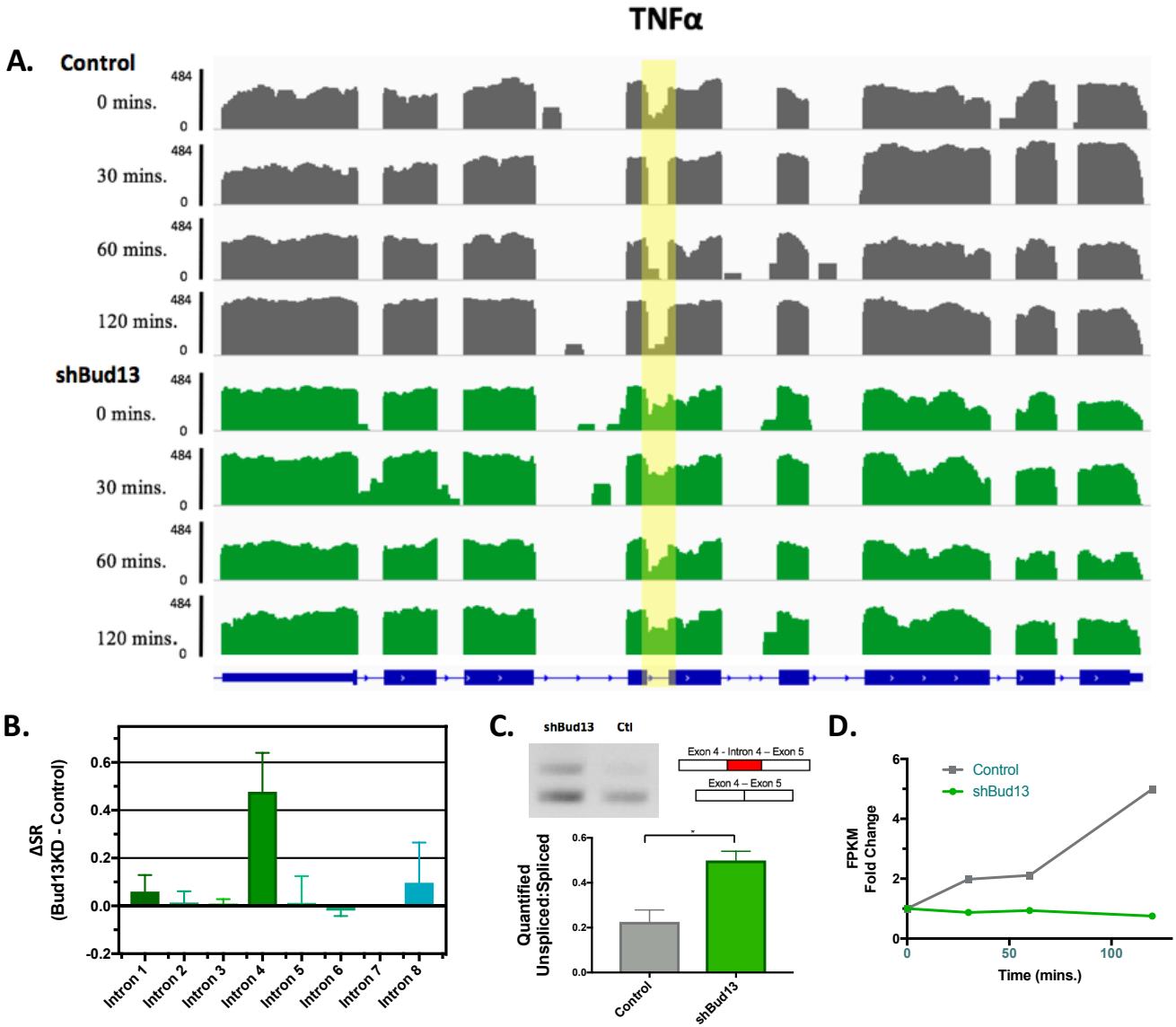

Figure 3: Bud13 knockdown leads to increased retention in the poorly splicing intron of Irf7

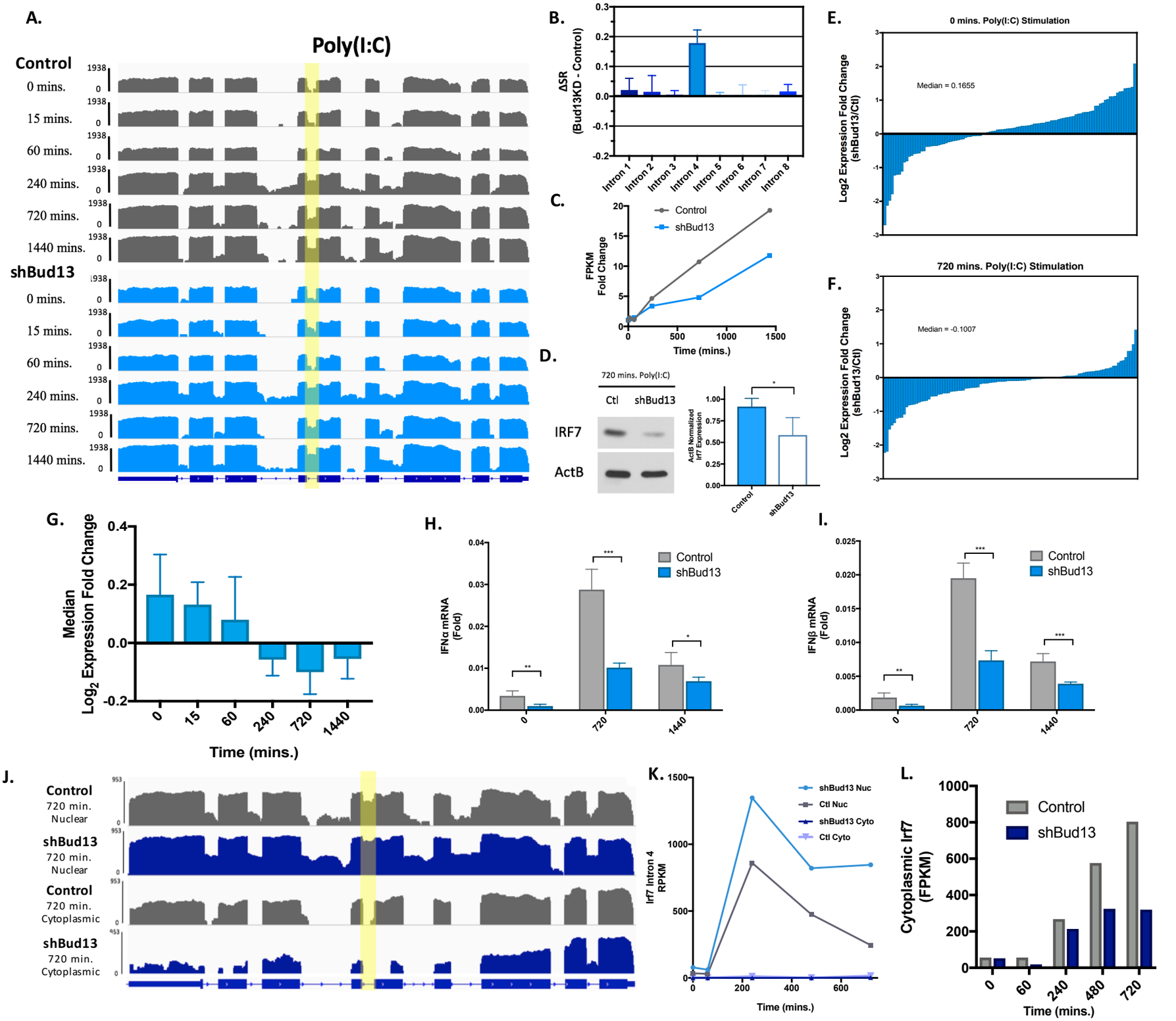

Figure 4: Bud13 knockdown alters the type I interferon response

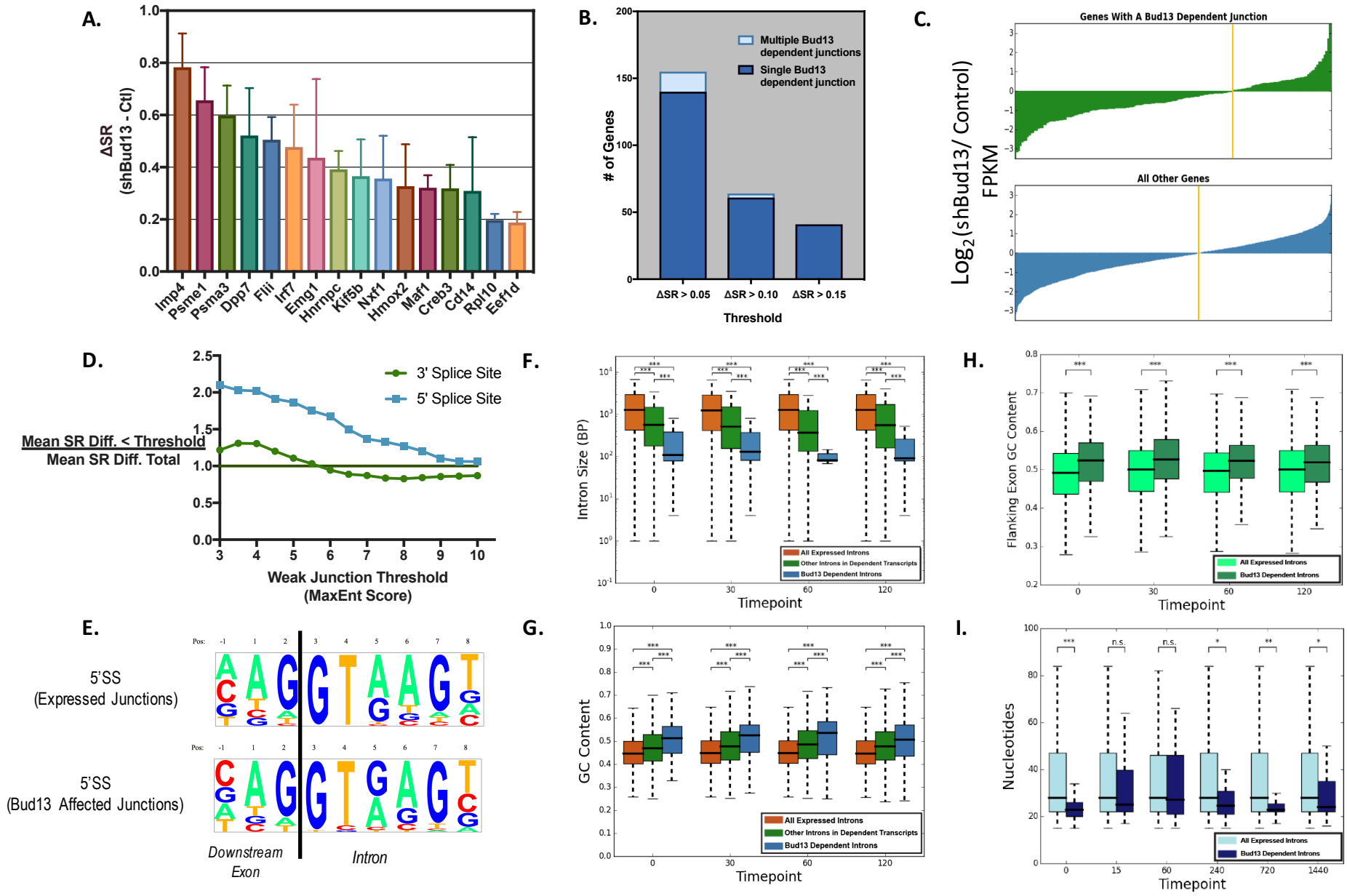

Figure 5: Global analysis of the role of Bud13.

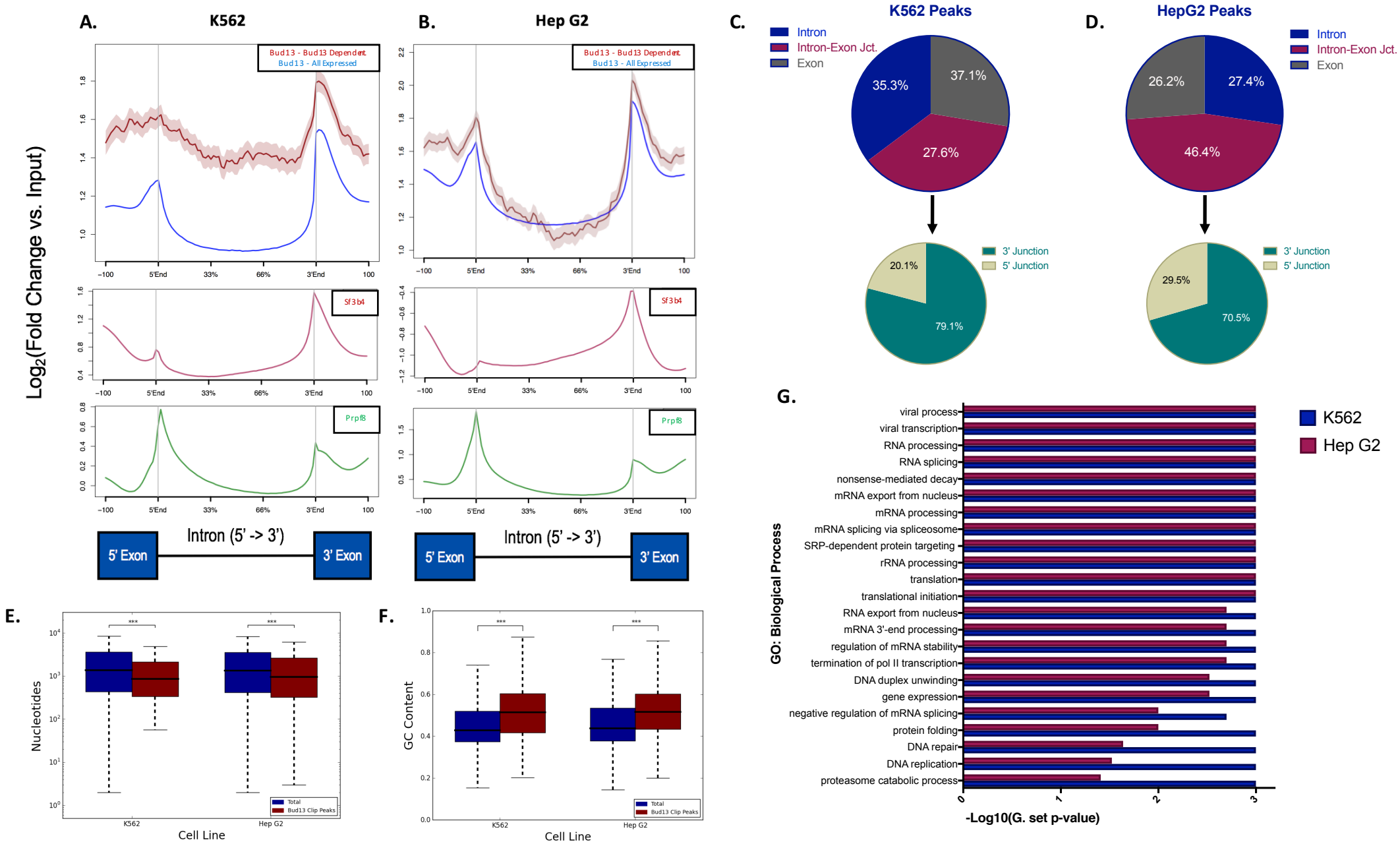

Figure 6: Bud13 interacts with Bud13 dependent junctions near the 3' splice site.

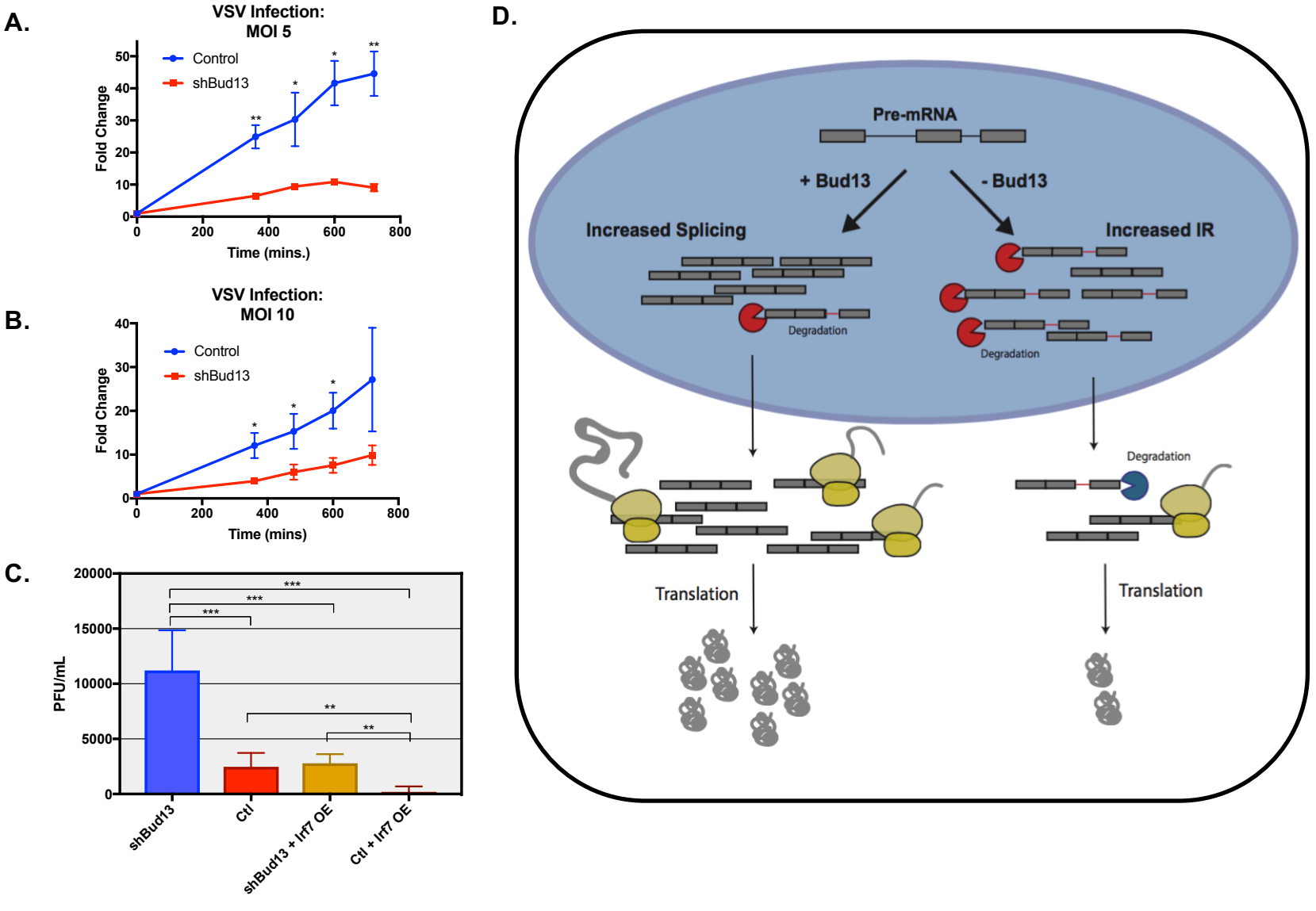

Figure 7: Bud13 knockdown alters the BMDM response to VSV.

FIGURE LEGENDS

Figure 1: *Irf7* contains a weak intron that is following many forms of stimulation. (A) Histogram of mapped reads corresponding to the TNFα-induced expression of Irf7. The poorly spliced fourth intron is highlighted. For all read density plots, reads are histogrammed in $\log_{10}$ scale and normalized to the maximum value across the stimulation. **(B)** Comparison of Irf7 splice donor and acceptor sites in mice, rats, and humans. **(C-F)** Histogram representing the intron length **(C),** intron GC content **(D)**, flanking exon GC content **(E)**, or 5' splice site strength of introns of expressed in BMDMs. Red represents location of Irf7 intron 4 **(C, D, F)** or upstream exon **(E)**. Black line represents downstream exon **(E)**. **(G, H)** Histogram of mapped reads corresponding to the IFNα **(G)** and poly(I:C) **(H)** induced expression of Irf7 focused on the slow splicing fourth intron. **(I)** Outline of Splicing Ratio (SR) metric. **(J)** Splicing ratio for all introns in Irf7 plotted against time stimulated with TNFα.

Figure 2: RAP-MS and RIP identifies Bud13 as an RNA binding protein that interacts with IRF7 mRNA. (A) Outline of the RAP-MS procedure used to identify RNA-binding proteins on transcritps of interest. **(B)** TMT ratio (Irf7/Actb) for proteins identified as enriched on either Irf7 (TMT ratio >1) or Actb (TMT ratio <1) transcripts. **(C)** RT-qPCR analysis of transcripts captured via RAP for Irf7 (blue) and Actb (gold) probes. **(D)** RIP followed by RT-qPCR for Irf7 and Rpl32 in TNFα stimulated BMDMs. Shown is the relative enrichment of transcripts captured in Bud13 RIP as compared to Rabbit IgG RIP. **(E)** Same as (d) except stimulation with poly(I:C). Data are representative of two independent experiments ((**C-E),** mean + SEM). *P < 0.05, **P < 0.01 and ***P < 0.001 (t-test).

Figure 3: Bud13 knockdown leads to increased retention in the poorly splicing intron of Irf7. (A) Histogram of mapped reads corresponding to the TNFα-induced expression of Irf7. The poorly spliced fourth intron is highlighted. shBud13 samples are shown in green. Control samples are shown in grey. **(B)** ΔSRs calculated for each junction in the Irf7 transcript. The ΔSR of intron 4 as compared to all other junctions is significant (Student's t-test, p<0.001). No other pairwise comparison is significant. **(C)** Splicing gel from RNA extracted from BMDMS stimulated for 30 mins. TNFα (top). Quantification of splicing gel (bottom). **(D)** Irf7 FPKM fold change with respect to time stimulated. shBud13 is shown in green, control is shown in grey. Data is representative of two independent experiments **(C)** and is represented as mean + SEM. * denotes p < 0.05, ** denotes p < 0.01, and *** denotes p < 0.001 using a Student's t test.

Figure 4: Bud13 knockdown alters the type I interferon response. (A) Histogram of mapped reads corresponding to the TNFα-induced expression of Irf7. The poorly spliced fourth intron is highlighted. shBud13 samples are shown in blue. Control samples are shown in grey. **(B)** ΔSRs calculated for each junction in the Irf7 transcript. The ΔSR of intron 4 as compared to all other junctions is significant (Student's t-test, p<0.001). No other pairwise comparison is significant. **(C)** Irf7 FPKM fold change with respect to time stimulated. shBud13 is shown in blue, control is shown in grey. **(D) I**mmunoblot analysis of Irf7 protein following 720 mins. poly(I:C) stimulation (left). Quantification relative to ActB (right). **(E)** Log_2 expression fold change (shBud13/control) for 119 ISGs in unstimulated BMDMs (median = 0.1655). **(F)** As in **(E)** for stimulated BMDMs (720 mins poly(I:C) (median = -0.1007). Wilcoxon rank-sum between **(E)** and **(F)**, *P*< .001. **(G)** Median $\log_2$ expression fold change (shBud13/control) for ISGs in unstimulated BMDMs, and BMDMs stimulated with Poly(I:C) 15, 60, 240, 720, and 1440 mins. Bars represent 95% CI. (Wilcoxon rank-sum, *P*< .001, for any of the 'early' time-points (0, 15, 60 mins) compared to any of the 'late' time-points (240, 720, 1440 mins). **(H)** RT-qPCR analysis of IFNα mRNA levels in unstimulated BMDMs and BMDMs stimulated with poly(I:C) for 720 mins and 1440 mins. **(I)** Same as **(H)** for IFNβ. **(J)** Nuclear fraction (top) and cytoplasmic fraction (bottom) histograms of mapped reads corresponding to the poly(I:C)-induced expression of Irf7 (720 mins). The poorly spliced fourth intron is highlighted. shBud13 samples are shown in blue. Control samples are shown in grey. Nuclear ΔSR = 0.35. **(K)** Nuclear and cytoplasmic RPKM for Irf7 intron 4 from fractionated BMDMs stimulated with poly(I:C). **(L)** Cytoplasmic Irf7 FPKM for control (grey) and shBud13 BMDMs stimulated with poly(I:C). Data is representative of four independent experiments **(H, I)** and is represented as mean + SEM. * denotes p < 0.05, ** denotes p < 0.01, and *** denotes p < 0.001 using a Student's t test. Results are presented relative to those of Rpl32 **(H,I).**

Figure 5: Global analysis of the role of Bud13. (**A)** Ranked bar chart showing genes with a junction most affected by Bud13 knock-down in all samples during TNFα stimulation. See S7 for histograms relating to most affected junctions. (**B)** Grouped bar chart depicting the number of genes that have a single Bud13 affected junction vs. multiple Bud13 affected junctions using three different ΔSR thresholds. **(C)** Transcripts were classified as 'Bud13 dependent' if they had a junction with a ΔSR. >0.15. The $\log_2$ expression fold change (FPKM shBud13/ FPKM control) for each gene represented by the transcripts in the 'Bud13 dependent' category as well as all other genes is shown. Median 'increased IR' = -0.5084. Median 'decreased IR' = -0.2170. (Wilcoxon rank-sum, $P < .01$). **(D)** Mean ΔSR. for junctions below the indicated threshold (x-axis) vs. mean ΔSR. for all junctions. Threshold applied for the 5' splice site (blue) and the 3' splice site (green). **(E)** 5'SS motif for all expressed junctions as compared to junctions that show retention upon Bud13 knockdown (ΔSR. > 0.15). **(F)** Size of intron for introns retained upon Bud13 knockdown (ΔSR. > 0.15) (blue), in introns located in the same transcript as those affected by Bud13 (green), and in introns from all expressed transcripts (orange). **(G)** Same as **(F)** for GC content. **(H)** Flanking exon GC content for exons that flank introns retained upon Bud13 knockdown (ΔSR. > 0.15) (dark green) as compared to exons that flank introns from all expressed transcripts (light green). **(I)** Distance from the branch point to the 3' splice site for introns retained upon Bud13 knockdown (ΔSR. > 0.15) (dark blue) as compared to introns from all expressed transcripts (light blue). **(F-I)** data from BMDM TNFα stimulation. Box plots show median (center line), interquartile range (box) and tenth and ninetieth percentiles. $*P < 0.05$, $**P < 0.01$ and $***P < 0.001$ (Mann-Whitney *U*-test).

Figure 6: Bud13 interacts primarily near the 3' splice site of small, GC rich introns. (A) eCLIP-seq read density plots in K562 cells. Bud13 density plot over all expressed junctions shown in blue (top), Bud13 density plot over Bud13 dependent junctions shown in red (top). Sf3b4 density plot over all expressed junctions shown in maroon (middle), and Prpf8 density plot over all expressed junctions is shown in green (bottom). **(B)** Same as in **(A)** but for Hep G2 cells. **(C)** Bud13 eCLIP-seq peak distribution. Peaks fell within either intronic regions, intron-exon junctions, or exonic regions. Peaks that fell within intron-exon junction were further classified as 5' junction peaks or 3' junction peaks (bottom). **(D)** Same as **(C)** but for Hep G2. **(E)** Size of all introns in expressed transcripts for the given cell line (dark blue) vs size of introns with overlapping eCLIP peak (maroon). Shown in K562 (left) and Hep G2 (right) cells. Box plots show median (center line), interquartile range (box) and tenth and ninetieth percentiles (whiskers). $*P < 0.05$, $**P < 0.01$ and $***P < 0.001$ (Mann-Whitney *U*-test). **(F)** Same as **(E)** for GC content. **(G)** GO terms (biological process) enriched among Bud13 eCLIP peaks in K562(dark blue) and Hep G2 (maroon) cells.

Figure 7: Bud13 knockdown alters the BMDM response to VSV. (A) RT-qPCR analysis of Irf7 mRNA levels in infected control or shBud13 BMDMs stimulated with VSV (MOI 5) across 24 hours. **(B)** Same as in **(A)** except stimulated at an MOI of 10. Results are presented relative to those of Rpl32. **(C)** PFU/mL for viral supernatant from infected shBud13 (blue), control (red), shBud13 with Irf7 overexpression (yellow), or control with Irf7 overexpression (maroon) BMDMs. Data is representative of two **(A, B)** or three independent experiments **(C)** and is shown as mean + SEM. * denotes $p < 0.05$, ** denotes $p < 0.01$, and *** denotes $p < 0.001$ using a Student's t test

SUPPLEMENTAL FIGURES

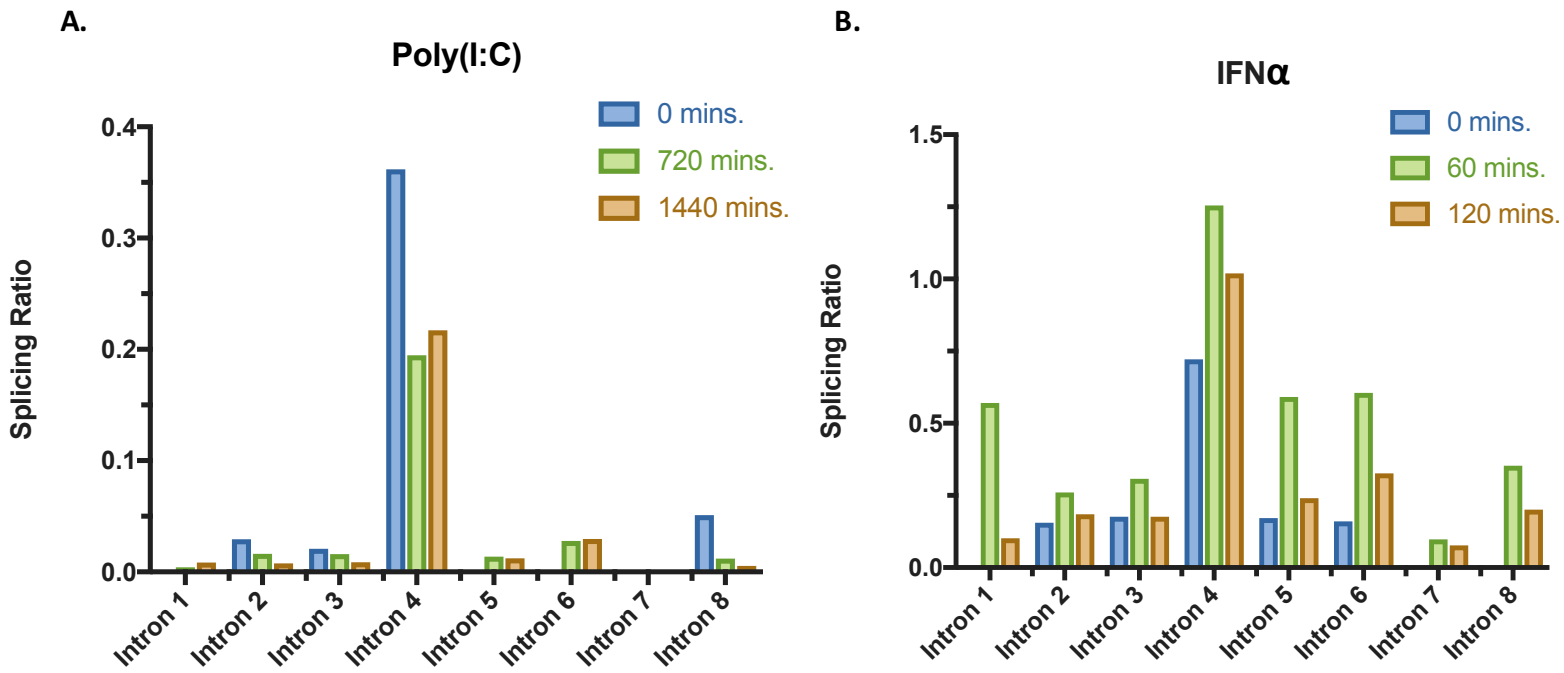

Figure S1: Splicing Ratios across all junctions in Irf7

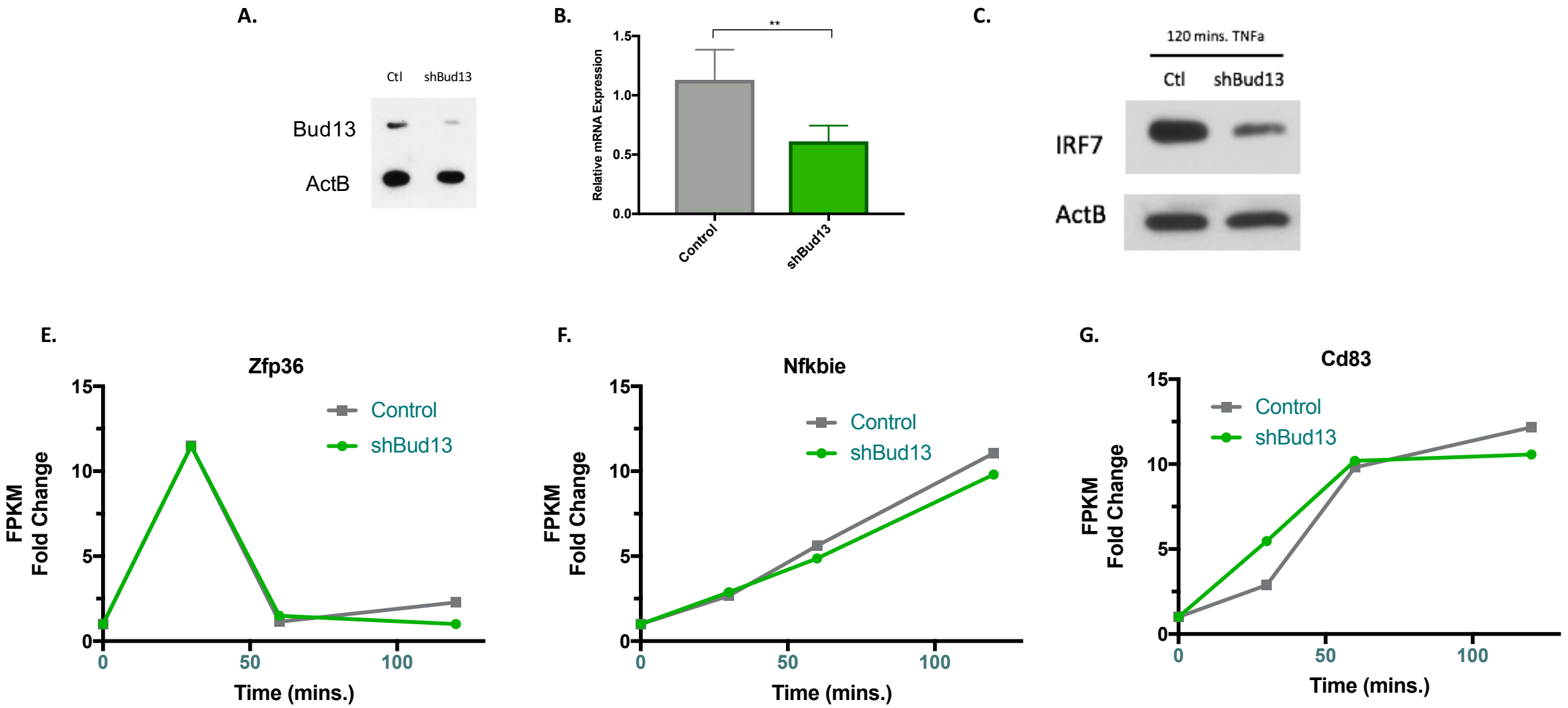

Figure S2: shBud13 knocks down Bud13 protein and mRNA.

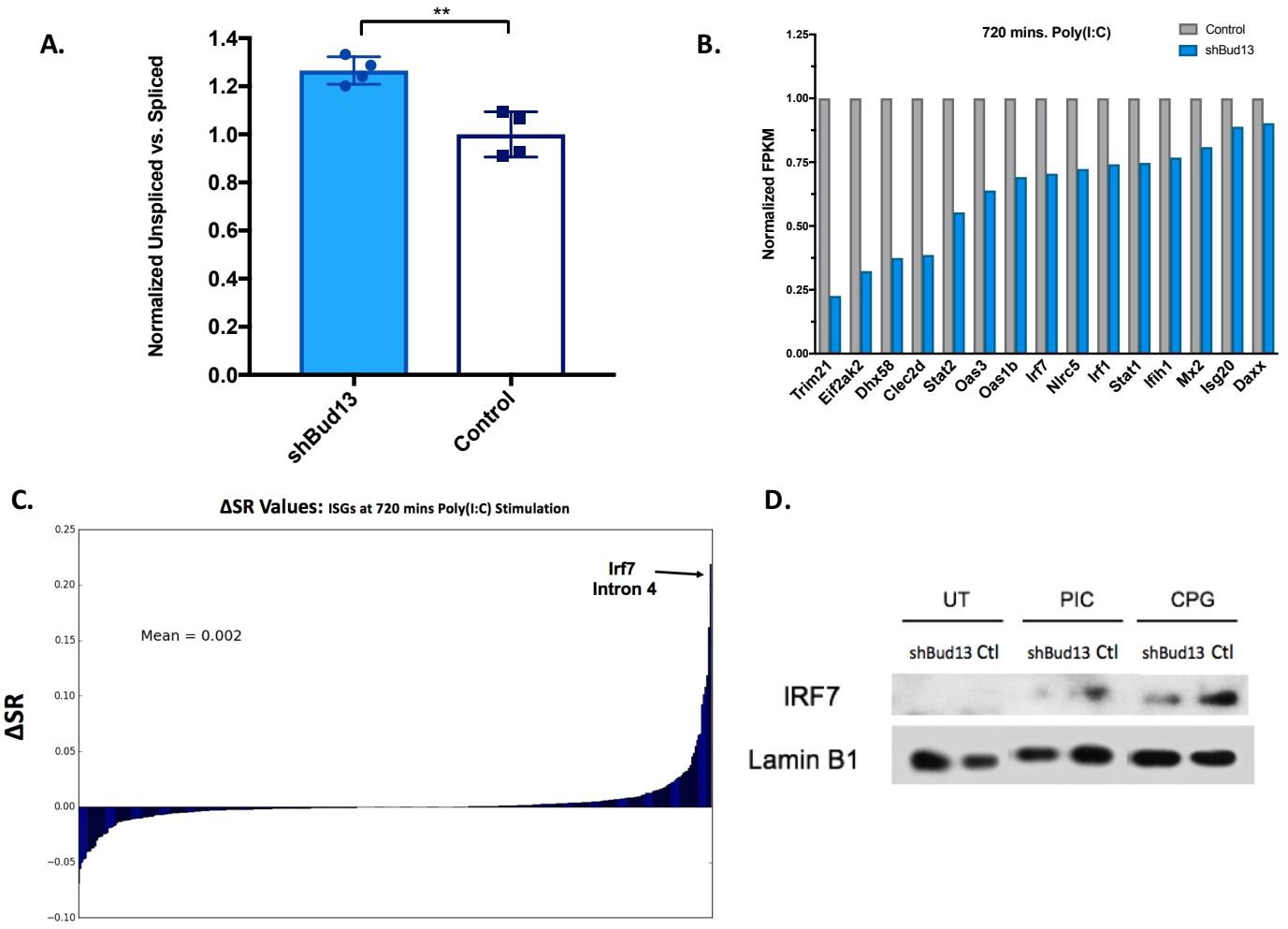

Figure S3: Irf7 Intron 4 is the most Bud13 knockdown affected junction of all ISGs.

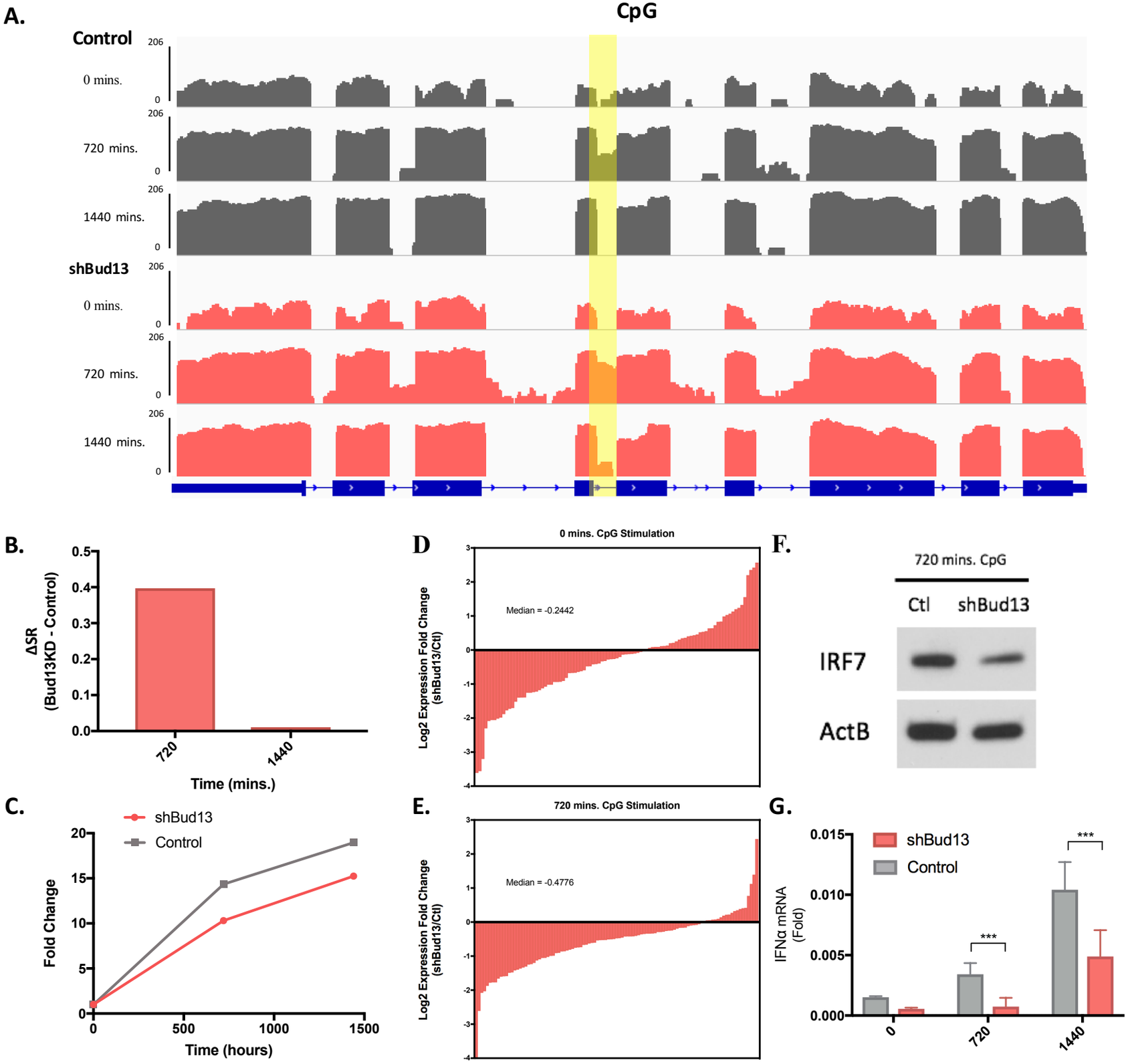

Figure S4: Bud13 knockdown alters the type I interferon response in response to CpG

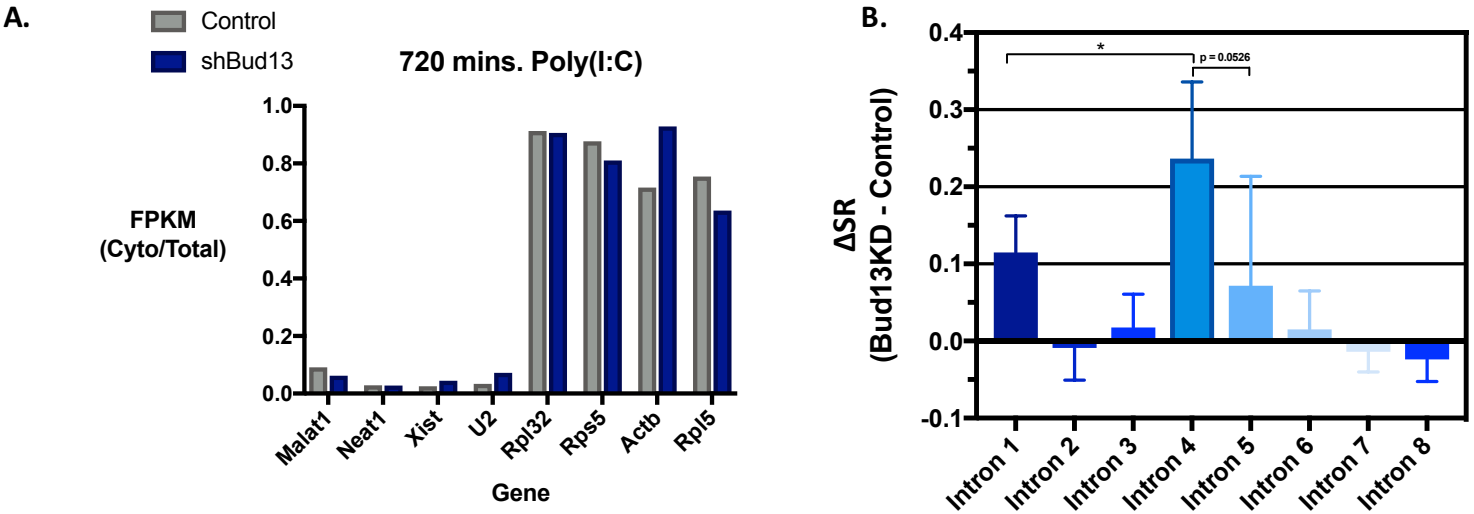

Figure S5: BMDM fractionation and effect of Bud13 on nuclear Irf7 splicing

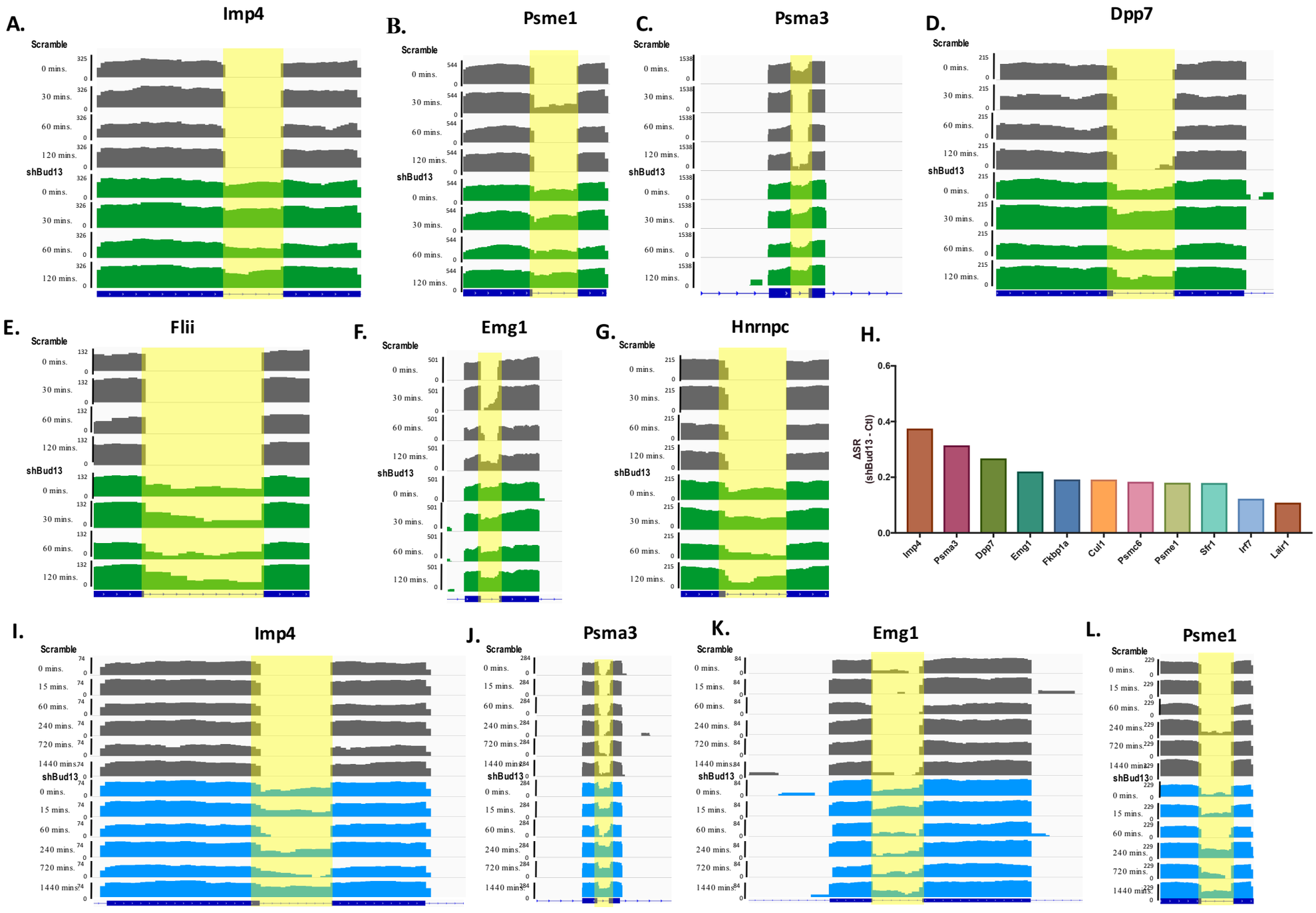

Figure S6: Histograms of mapped reads corresponding to hits identified in TNFα and PIC data-sets.

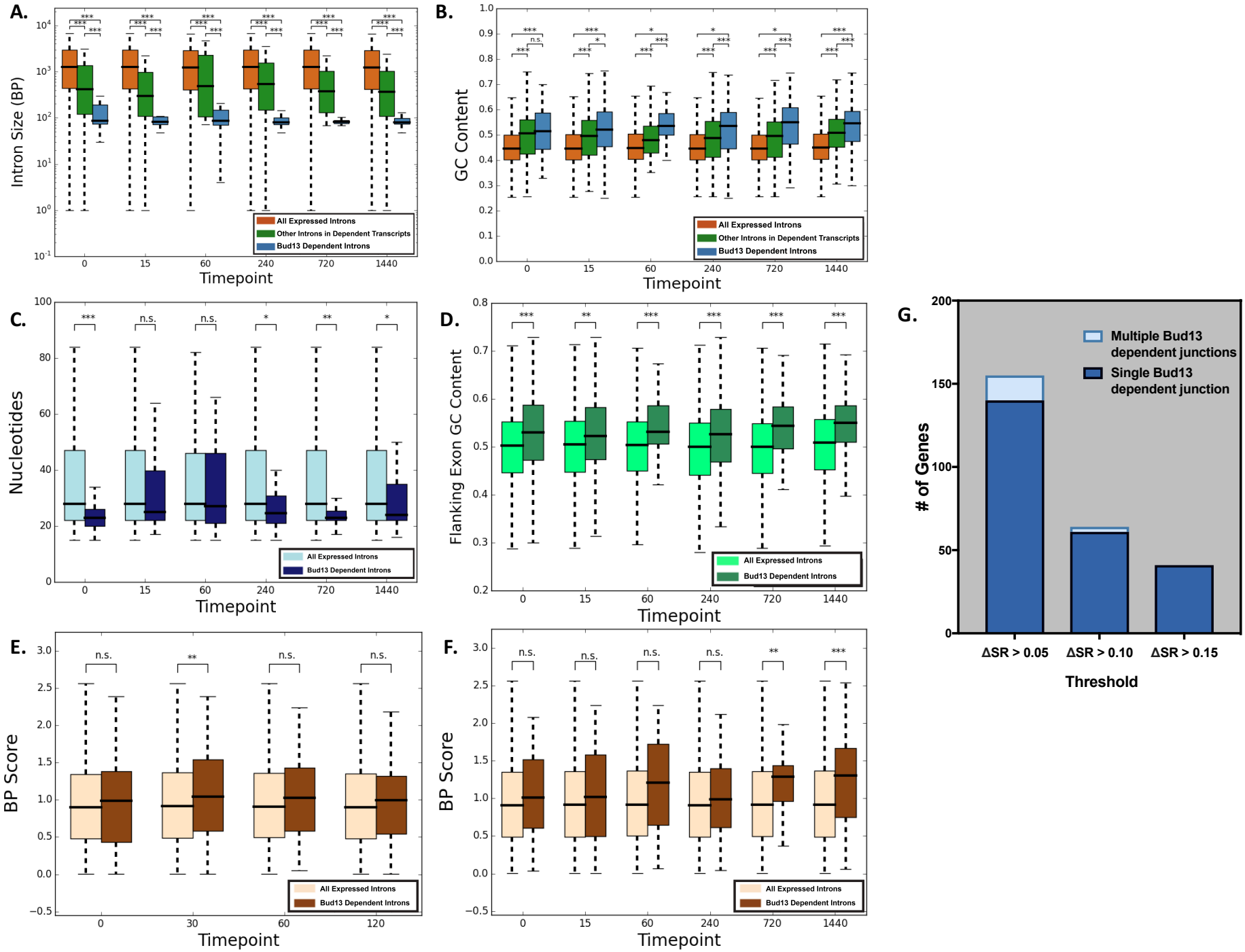

Figure S7: Supplemental global analysis of shBud13

A.

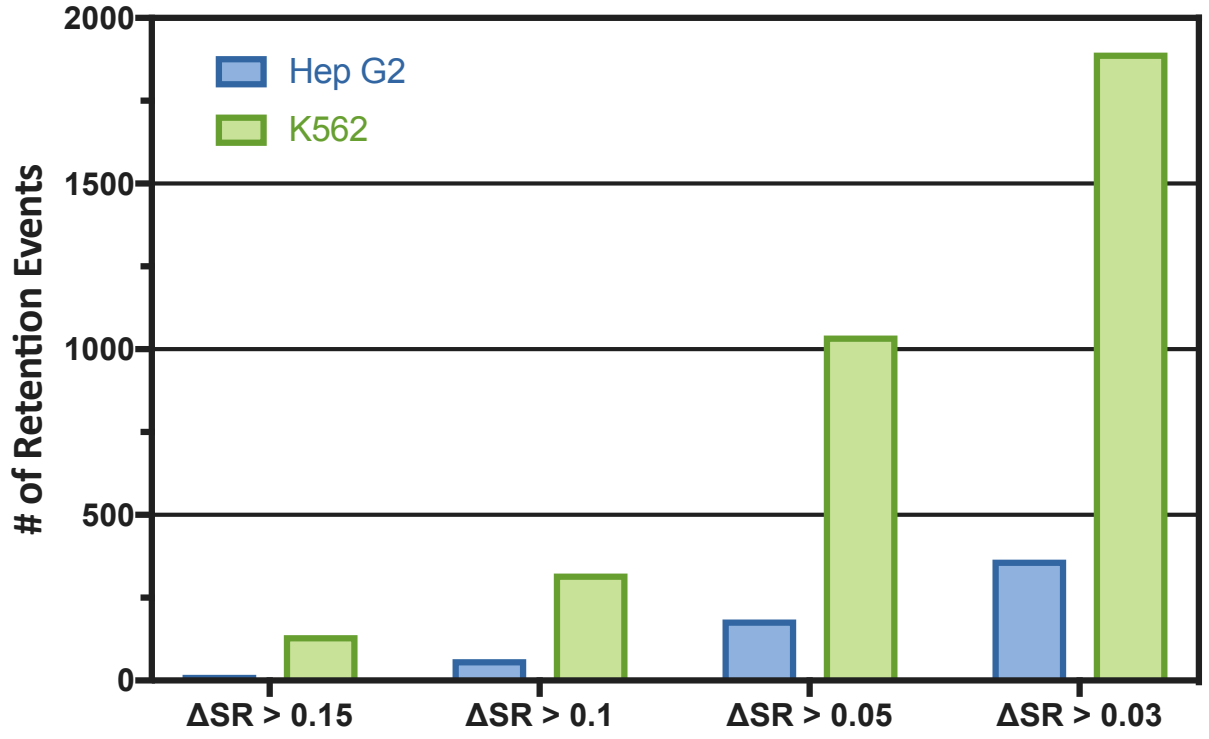

Figure S8: Bud13 dependent IR events in Hep G2 and K562 cells.

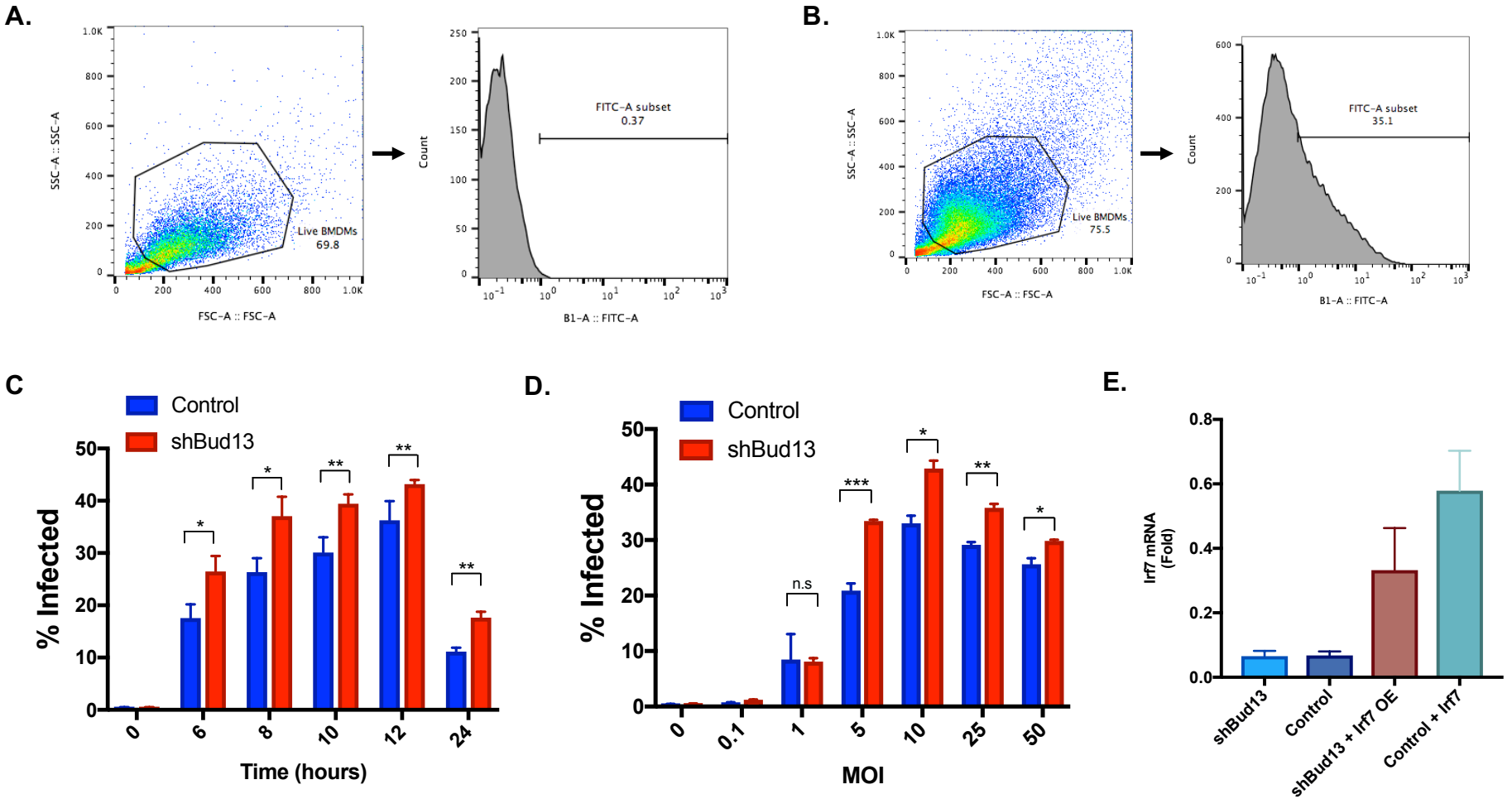

Figure S9: Bud13 knockdown alters the BMDM infection via VSV.

A.

B.

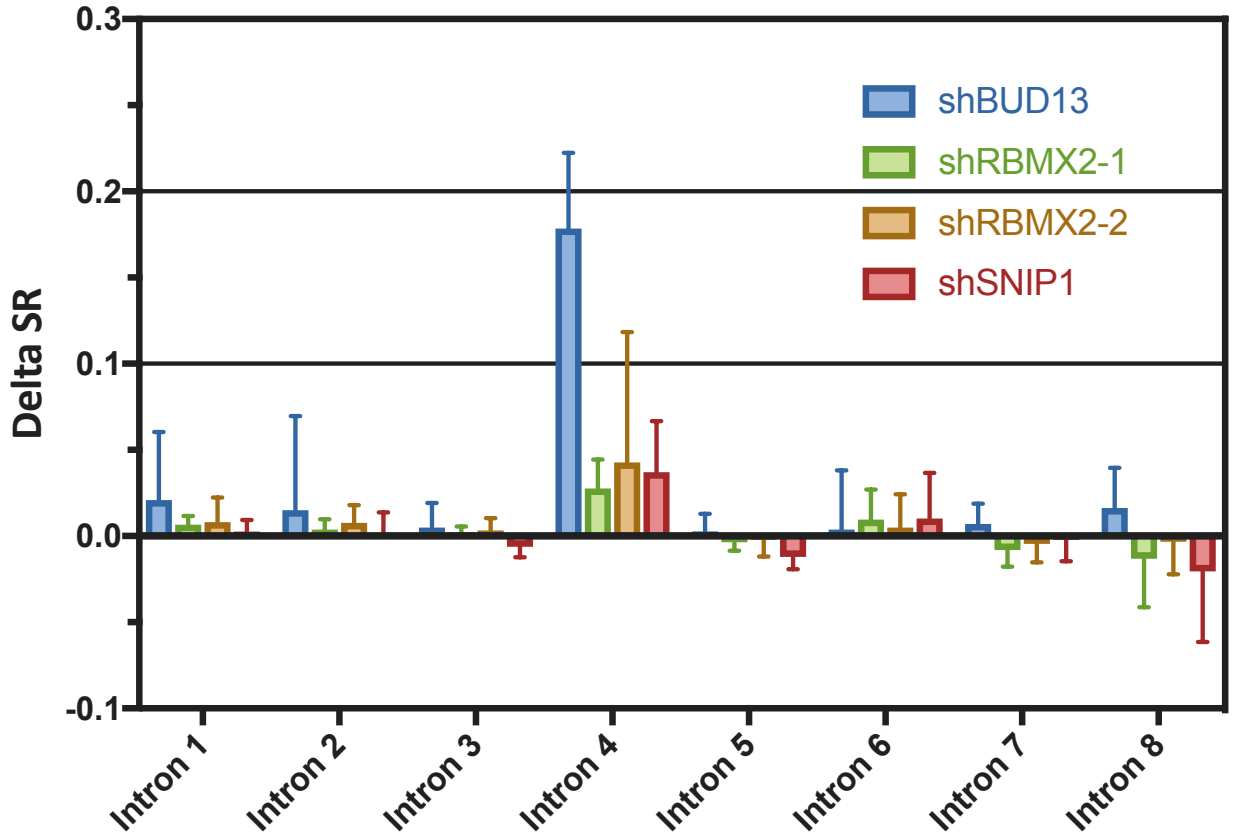

C.

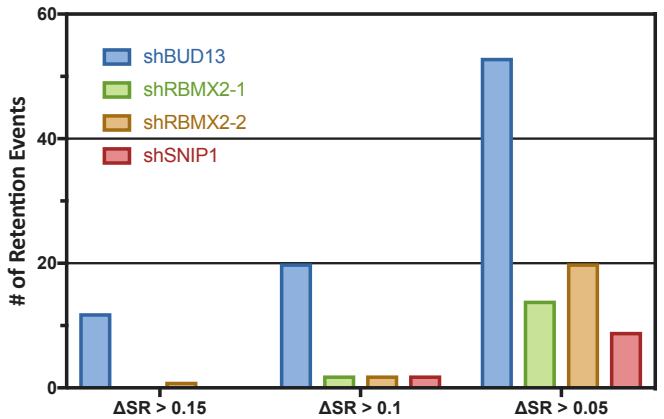

Figure S10: Knockdown of other RES complex proteins.